The Herschel Catalogue of Solar System Object Observations Explanatory Supplement

Volume II

Version: 1.0
December 21, 2018

The Herschel Catalogue of Solar System Object Observations

Explanatory Supplement

Volume II

Prepared by:

Cristina Romero Calvo[1,2], Mark Kidger[1], Miriam Rengel[1,3,4] and Mircea Stoica[5].

1. Herschel Science Centre, European Space Agency, European Space Astronomy Centre.
2. Technische Universität Berlin, Germany.
3. Max-Planck-Institut für Sonnensystemforschung, Germany.
4. European Organisation for the Exploitation of Meteorological Satellites.
5. University Medical Center Hamburg-Eppendorf, Department of Neurophysiology and Pathophysiology, Hamburg, Germany.

Version: 1.0
December 21, 2018

Abstract

We present the second volume of the Herschel Catalogue of Solar System Object Observations (HCSSO). This has been prepared as a complement to the two catalogues of Herschel point source observations: The Herschel/SPIRE Point Source Catalogue (HSPSC) and the Herschel/PACS Point Source Catalogue (HPPSC), which filter and exclude moving targets.

The European Space Agency's Herschel Space Observatory has been the only space facility to date to cover a spectral range from the far infrared to sub-millimetre (55-672 μm). Herschel performed photometry and spectroscopy with its 3 on-board instruments: 2 diffraction-limited cameras - PACS (simultaneous observations in 70 μm or 100 μm and 160 μm) and SPIRE (simultaneous observations in 250 μm, 350 μm and 500 μm), each with a low-to-medium resolution spectrograph and a very high resolution heterodyne spectrometer, HIFI. These three instruments were designed to meet the goals of the mission to study the formation of stars and galaxies, physics of the interstellar medium, astrochemistry and solar system research.

Herschel performed around 37000 science observations of which 1692 were of Solar System objects (4.5% of the total) which represent 170 individual objects, including 5 planets and 6 of their satellites, 14 comets, 107 TNOs and 38 other asteroids. These measurements have been only partially exploited and to facilitate their analysis we have compiled these observations in the Herschel Catalogue of Solar System Object Observations (SSOO). We have included a detailed classification of the observed bodies, a complete ancillary information as well as physical circumstances of the observations (phase angle, heliocentric distance, etc.) to facilitate a search for correlations between properties.

In order to provide further information of interest we analysed 1287 photometric observations from PACS. We used the science ready maps in the Herschel Interactive Processing Environment (HIPE) v15.0.0 and due to the diversity of the 170 SSOs (e.g. TNOs, planets) we had to developed a pipeline for applying point source aperture photometry to the different bodies. The quality of the measurements had been analysed taking into account the source flux, sky background and published results from different types of bodies and flux densities of SSO.

Contents

List of Figures **7**

List of Tables **8**

1 Introduction **10**
1.1 Motivation . . . 10
1.2 Objective . . . 10
1.3 Scope . . . 10
1.4 Notes . . . 11

2 Herschel Space Observatory **12**
2.1 Mission overview . . . 12
2.2 Instruments . . . 13
2.3 Astronomical Observation Templates . . . 15
2.4 Herschel Data Products . . . 16
2.5 Herschel Interactive Processing Environment . . . 17

3 Catalogue Description **18**
3.1 Compilation of the Observations . . . 18
3.2 Organization of the Information . . . 23
3.2.1 Classification of the Targets . . . 23
3.2.2 Ancillary Information . . . 24
3.2.3 Physical Circumstances . . . 25
3.2.4 Example . . . 27
3.3 Listing of column headings used . . . 28

4 Completion of Missing Information: Photometric Calculation **31**
4.1 Scan Map and Mini Scan Map/Point Source . . . 31
4.1.1 Photometric Calculation Pipeline . . . 33
4.1.2 Validation of the Pipeline . . . 42
4.1.3 Flux Consolidation Pipeline . . . 47
4.1.4 Validation of the Consolidation of Fluxes . . . 49
4.2 Images Included in the Catalogue . . . 52

5 Results **53**
5.1 General Analysis of the Catalogue Data . . . 53
5.2 Conclusions . . . 56
5.3 Problems Encountered . . . 56
5.3.1 Sky Contamination . . . 57
5.3.2 Faint Bodies . . . 58
5.3.3 Eliminated Observations . . . 59

References **61**

Appendix **72**

A List of Acronyms **72**

B Index Publications of Herschel Observations **74**

List of Figures

1 Herschel space observatory. Ref. [7]. 12
2 Herschel instruments. Ref. [8]. 14
3 Percentage of Solar System Objects and their observations. Although Minor Planets (including TNOs) make up 80% of observed SSOs, they make up only 65% of the AORs. In contrast, Major Planets make up just 3% of the SSO targets observed, but form 12% of the AORs. 21
4 Percentage of minor planets objects and their observations. 22
5 Percentage of TNOs and their observations. 22
6 Photometric calculation pipeline. 33
7 Example of observed body outside the map due to a programmed offset in target coordinates. 34
8 Comparison between coordinates - similar results. 35
9 Comparison between coordinates - different results 1. 35
10 Comparison between coordinates - different results 2. The arrow indicates the projected direction of the comet towards the Sun. Observation: 103P/Hartley 2 - ObsID: 1342209385 - HPPUNIMAPB. 36
11 Source fitting example for an extended source. The arrow indicates the projected direction of the comet towards the Sun. Observation: 103P/Hartley 2 - ObsID: 1342209385 - HPPUNIMAPB. 37
12 Aperture photometry example for a point source. 38
13 Flux STD calculation - grid. 41
14 Flux STD calculation - plot fluxes. 41
15 Flux STD calculation - grid after exclusion of apertures by sigma clipping. . 42
16 Fluxes vs cumulative errors resulting from the differences between calculated and published fluxes. 43
17 Top graphics: comparison between the 70 μm flux density estimates from the HPPSC and this work (left) and from the HPPSC and those presented in the literature (right), the black dashed lines represent the fitted regression line for each dataset. Bottom graphics: difference in percentage for each data set. The black horizontal lines indicate the thresholds of $\pm$15% between the two fluxes. 44
18 Top graphics: comparison between the 100 μm flux density estimates from the HPPSC and this work (left) and from the HPPSC and those presented in the literature (right), the black dashed lines represent the fitted regression line for each dataset. Bottom graphics: difference in percentage for each data set. The black horizontal lines indicate the thresholds of $\pm$15% between the two fluxes. 45
19 Top graphics: comparison between the 160 μm flux density estimates from the HPPSC and this work (left) and from the HPPSC and those presented in the literature (right), the black dashed lines represent the fitted regression line for each dataset. Bottom graphics: difference in percentage for each data set. The black horizontal lines indicate the thresholds of $\pm$15%. 46
20 Contaminated sky in the observation of Pluto at a wavelength of 160 μm. . 47
21 Flux consolidation pipeline. 47

22 Top graphic: comparison between the 70 μm flux density estimates from this work and those presented in the literature, the black dashed lines represent the fitted regression line for the dataset. Bottom graphic: difference in percentage for the data set. The black horizontal lines indicate the thresholds ±15% agreement. 50
23 Top graphic: comparison between the 100 μm flux density estimates from this work and those presented in the literature, the black dashed lines represent the fitted regression line for the dataset. Bottom graphic: difference in percentage for the data set. The black horizontal lines indicate the thresholds ±15% agreement. 50
24 Top graphic: comparison between the 160 μm flux density estimates from this work and those presented in the literature, the black dashed lines represent the fitted regression line for the dataset. Bottom graphic: difference in percentage for the data set. The black horizontal lines indicate the thresholds ±15%. 51
25 Comparison of the SSOO - calculated temperature vs heliocentric distance. (A) All observations, major class type. (B) Minor planets, dynamical class. (C) TNOs, second dynamical class. (D) TNOs between 23 and 52 AU, main cluster in (C). We see the expected correlation, although there are some outliers. 53
26 Comparison of the SSOO - albedo vs heliocentric distance. (A) All observations, major class type. (B) Minor planets, dynamical class. (C) TNOs, second dynamical class. (D) TNOs between 23 and 52 AU, main cluster in (C). 54
27 Comparison of the SSOO - colour indexes vs albedo. (A) Minor planets, dynamical class. (B) Minor planets, dynamical class. 55
28 Comparison of the SSOO - colour indexes vs temperature. (A) B-V against temperature for Minor planets, split by dynamical class. (B) V-R for Minor planets, split by dynamical class. 55
29 Example of sky contamination - identifying the source. 57
30 Example of sky contamination - aperture photometry. 57
31 Example of sky contamination - extraction of the contamination. 58
32 Eliminated observations - 1999 CD158 - ObsIDs: 1342206024 / 1342206025. 59
33 Eliminated observations - 136199 Eris - ObsID: 1342224854. 60
34 Eliminated observations - 2005 YU55 - ObsIDs: 1342232729 / 1342232730. . 60

List of Tables

1 Minor planets - Centaurs. 19
2 Minor planets - TNOs - Classical. 20
3 Minor planets - TNOs - Resonants. 20
4 Minor planets - Remaining TNOs. 21
5 Column information: classification of the targets - part 1. 23
6 Column information: classification of the targets - part 2. 23
7 Column information: ancillary information - part 1. 24
8 Column information: ancillary information - part 2. 24
9 Column information: physical circumstances - part 1. 25
10 Column information: physical circumstances - part 2. 25
11 Column information: physical circumstances - part 3. 25

12 Column information: physical circumstances - part 4. 25
13 Example: classification of the targets - part 1. 27
14 Example: classification of the targets - part 2. 27
15 Example: ancillary information - part 1. 27
16 Example: ancillary information - part 2. 27
17 Example: ancillary information - part 3. 27
18 Example: physical circumstances - part 1. 27
19 Example: physical circumstances - part 2. 27
20 Example: physical circumstances - part 3. 28
21 Example: physical circumstances - part 4. 28
22 Example: physical circumstances - part 5. 28
23 Example: physical circumstances - part 6. 28
24 Comparison between calculated and meta-data coordinates. 36
25 Beam FWHM for the most common mode of PACS. 37
26 Colour correction indexes. 40
27 Total number of targets and observations after pipeline for flux validation. . 48
28 List of targets with new fluxes observed at 70 μm. 48
29 List of targets with new fluxes observed at 100 μm. 49
30 List of targets with new fluxes observed at 160 μm. 49
31 Comparison of the SSOO - temperature vs heliocentric distance - statistics. 53
32 Comparison of the SSOO - albedo vs heliocentric distance - statistics. . . . 54
33 Comparison of the SSOO - colour indexes vs albedo - statistics. 55
34 Comparison of the SSOO - colour index vs temperature - statistics. 56

1 Introduction

1.1 Motivation

The Herschel Space Observatory was the fourth cornerstone mission in the European Space Agency's (ESA's) Horizon2000 science program following SOHO/Cluster II, XMM-Newton and Rosetta. Herschel was the first space observatory to operate from 55-672 μm, giving coverage from far-infrared to submillimetre wavelengths. Herschel explored the cold Universe for almost four years (from May 14, 2009 to April 29, 2013). With its 3.5-m diameter Cassegrain telescope, it is the largest telescope ever deployed in space.

The key science objectives of the mission as stated in *Herschel's mission overview* [9], emphasise the formation of stars and galaxies, and the interrelation between the two, but also includes the physics of the interstellar medium, astrochemistry, and solar system studies.

This catalogue focused on the science objective of studying the Solar System. Herschel made 1763 individual observations of Solar System objects, an observation archive so-far only partially exploited and with potential for new scientific discoveries.

1.2 Objective

The aim of this work was to use all the Solar System science observations to create the Herschel Catalogue of Solar System Object Observations (HCSSOO) of which the goal is for it to become a reference archive from which information may be extracted selecting by type (e.g. object class, albedo, colour index) for comparative statistical studies and further exploitation of the data.

1.3 Scope

Herschel produced 1692 good quality SSOO. The observations were made by two imaging cameras/medium resolution spectrometers covering the following wavelengths: PACS (55-210 μm) SPIRE (191-672 μm) and a very high resolution heterodyne spectrometer HIFI (157-625 μm).

All these observations are included in the catalogue, the creation of which consisted of 4 steps:

1. Compilation of the Herschel Catalogue of Solar System Object Observations.

   1692 science observations of 170 different bodies, including Major Planets, Minor Planets: Near-Earth Objects (NEOs), Main Belt Asteroids (MBAs), Centaurs, Trans-Neptunian Objects (TNOs), Satellites and Comets are compiled into the HCSSOO. The process of compilation also involved the analysis of 63 available publications which presented Herschel observations of the Solar System.

2. Organization of the information in order to facilitate its accessibility and retrieval.

   In order to have a catalogue that is as complete as possible, different types of information had to be gathered. This information has been divided into three parts for purposes of giving background information on the target:

(a) Classification of the observed bodies to facilitate defining samples

This section includes the following information: NAIF id, International Astronomical Union nomenclature, target, commonly-used alternative names, first classification, dynamical classification, second dynamical classification, classification comment.

(b) Complete ancillary information for each SSOO

The following data is included: Observation ID, operation day, start time, integration time, scientist proposal, scientific mode, instrument and band wavelength.

(c) Physical circumstances for each SSOO

In this section, we include the published data (published flux and its standard deviation and the method of flux calculation used), as well as both the physical circumstances for each solar system object observed (right ascension and declination, illumination, heliocentric range, observer range, phase) and useful ancillary data such as albedo and its standard deviation, V-R, B-V colour indexes and their errors, that help to provide context for the Herschel data.

3. Completion of the missing information in the catalogue.

In order to maintain homogeneity in the catalogue and to provide further information of interest a photometric study we carry out using PACS observations. The Herschel Interactive Processing Environment (HIPE) v15.0.0 was used to analyse science ready maps and to follow a pipeline for which its main basic operations were:

(a) Source fitting of the body

(b) Annular sky aperture photometry

(c) Photometric aperture correction

(d) Colour correction

The final result is the monochromatic colour corrected (CC) flux density. The quality of the measurements was analysed taking into account the source flux, sky background and published results from different types of bodies and flux densities of SSO.

4. Catalogue dissemination and preserving it as part of the Herschel Legacy Archive.

We aim to facilitate the analysis of Herschel SSO data and help the scientific community to use the archive to widen our knowledge of the Solar System.

1.4 Notes

The primary goal of the catalogue is to provide reliable bulk information that can be for scientific studies. Therefore, a detailed information of the data description, methodology and quality assessment can be found in this explanatory supplement: users are advised to study this information carefully when using the data ensemble for statistical studies.

2 Herschel Space Observatory

The Herschel Space Observatory was the fourth cornerstone mission in the European Space Agency's Horizon2000 science program. Herschel was the first space observatory to operate from 52 μm to 672 μm, giving coverage from far-infrared to submillimetre wavelengths, which has never been done before. The observatory was named after Sir William Herschel who discovered infrared radiation in 1800.

2.1 Mission overview

After launch, on 14 May 2009, initial commissioning, cooling and mirror opening, Herschel operated successfully from June 2009 to 29 April 2013 [87]. It carried a 3.5m diameter primary mirror in a passively cooled Cassegrain telescope: the largest infrared telescope ever deployed in space. Its dimensions allowed a unique spatial resolution and sensitivity at far-infrared and sub-millimetre (sub-mm) wavelengths, see Figure 1. The mission finished when Herschel ran out of the cooling liquid helium that was necessary to maintain the operational temperatures for the instruments' detectors [5], [42].

Figure 1: Herschel space observatory. Ref. [7].

Herschel was located at the L2 Lagrangian point, allowing it to minimise scattered light from the Sun, the Earth and the Moon, all powerful infrared sources, which were all in the sunward area of the sky, as Herschel effectively had its back towards them, leaving them either behind the sunshield or, at worst, (almost always) within the Sun exclusion zone in the sky. [22]. The satellite had a mass of 3400 kg at launch and was 7.5m high and 4m x 4m overall cross section [7].

The main mission objectives of the Herschel space observatory as described in the *"Herschel Mission Overview and Key Programmes"* [10], consisted of performing:

1. *Wide-area photometric surveys of the extragalactic and galactic sky.*

To measure dust-enshrouded star formation activity throughout cosmic time and in our own nearby galaxies today.

2. *Detailed studies of the physics and chemistry of the interstellar medium.*
   Both locally in our own galaxy as well as external galaxies by means of photometric and spectroscopic surveys.

3. *Observational astrochemistry of gas and dust as a quantitative tool for understanding the stellar/interstellar life-cycle.*
   Investigating the physical and chemical process involved in star formation, early and late stages in stellar evolution including gas and dust disk around young and mature stars.

4. *Spectroscopic and photometric study of solar system objects and their atmospheres.*
   Also crucial as calibration sources.

The cold mission lifetime of Herschel was planned to be of 3.5 years, of which 0.5 years was to be taken up with commissioning and performance verification (PV), although the cryogen lasted almost four years. The observing time of Herschel consisted of Guaranteed Time (GT) which used around 32% of the time, owned by contributors to the Herschel mission, and the remaining was for Open Time (OT) which was open for scientists' proposals and for Director's Discretionary Time (DDT) for urgent observing requests that could not be covered by the previous mentioned proposals. Over 37000 science observations were made during the more than 25000 hours of science time, while approximately 10000 PV and calibration observations of science quality were also made in standard science modes, making a total of ≈47000 science observations in the Herschel Science Archive. The Herschel observation programs and the time dedicated for each of them can be found in [12] and [11].

2.2 Instruments

The telescope focussed the light onto the three instruments: PACS, SPIRE and HIFI, see Figure 2. These instruments complement each other, performing photometry in six bands with centre wavelengths of 70, 100, 160 μm for PACS and 250, 350 and 500 μm for SPIRE and spectroscopy over the full Herschel wavelength coverage [86].

1. **PACS**

   The Photodetector Array Camera and Spectrometer (PACS) had two sub-instruments, which are described in the *"Herschel Explanatory Supplement vol. III: The Photodetector Array Camera and Spectrometer (PACS) Handbook"* [91]:

   - An imaging dual-band photometer operating over an instantaneous field of view (FoV) of 3.50 × 1.750 arc-minutes, with full sampling of the telescope point spread function [91]. With two different simultaneous wavelength observations: one with a blue/red filter observing at 70 μm and 160 μm; a second one with a green/red filter observing at 100 μm and 160 μm.

   - A medium resolution integral-field spectrograph operating between 51-210 μm with a field of view of 47 × 47 arc-seconds [91].

2. **SPIRE**

   Spectral and Photometric Imaging Receiver (SPIRE) was designed to exploit the advantages of the Herschel Space Observatory for observations in the poorly explored 200-700 μm range. It was divided in two sub-instruments, which are described in *"Herschel Explanatory Supplement vol. IV: The Herschel-SPIRE instrument and its in-flight performance"* [45]:

   - A three-band imaging photometer which carried three spectral bands centred on approximately 250, 350 and 500 μm with a FoV of 4×8 arc-minutes.
   - An imaging Fourier-transform spectrometer that used two overlapping bands to cover 194-671 μm and with a circular FoV of 2 arc-minutes.

3. **HIFI**

   Heterodyne Instrument for the Far Infrared (HIFI), with its high spectral resolution observed and identified with a unique level of detail, molecular species in space and studied their properties e.g. (motion, temperature).

   HIFI was a very high-resolution heterodyne spectrometer. Heterodyning is a signal processing technique used to translate the frequency range that is being observed to a lower frequency range where is easier to perform measurements. HIFI observed in seven bands covering the wavelength range of 157-625 μm. Bands from one to five gave continuous coverage from 240-625 μm and used a Superconductor-Insulator-Superconductor(SIS) mixers. Bands six and seven covered the 157-210 μm and used Hot Electron Bolometer (HEB) mixers [23].

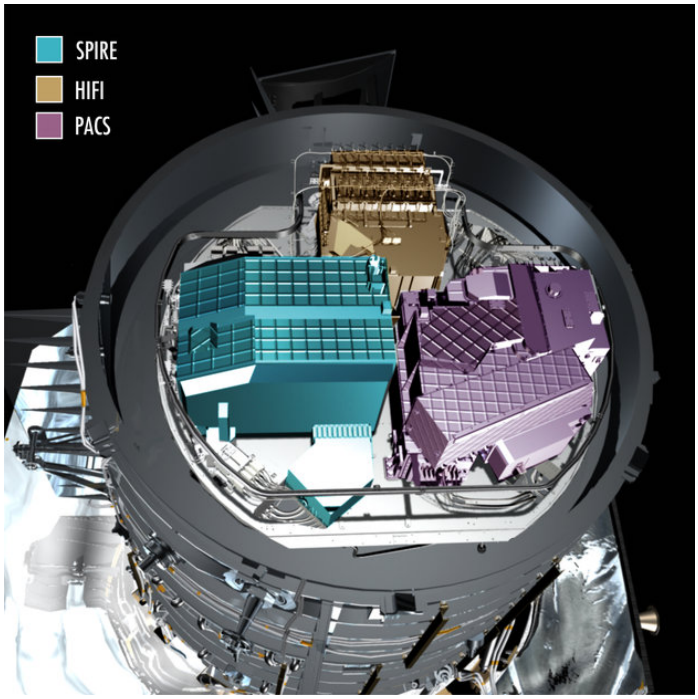

Figure 2: Herschel instruments. Ref. [8].

2.3 Astronomical Observation Templates

Astronomical Observation Templates (AOTs) are described in ESA's Herschel documentation [6] *"a standard observing mode with an instrument that can be translated into instructions for the spacecraft to carry out the observations autonomously."* This means that when a scientist requested an observation first an instrument was chosen and then a suitable AOT for that instrument, since only pre-defined types of observation were carried out. Each AOT had its permitted sub-modes, each with a number of parameters that could be set by the astronomer to personalise the observation, converting the AOT into an Astronomical Observation Request (AOR), which represented the final parameters that were required to attain the science goals of the observation.

These were the three instruments' AOTs [38], [91], [102], [100]:

PACS

1. Photometry: there could be three types:
   - The scan map and Mini scan map/point-source photometry: The scan map, was the most used AOT, it consisted of scanning over a requested region in the sky with the telescope. Two observations (scan and cross-scan) were performed at orthogonal scan angles in order to provide a good sensitivity and even coverage. The mini scan map was similar to the scan map AOT, but its purpose was mostly point sources with a uniform coverage over a 50 arc-seconds area of sky. The mini-scanmap worked most efficiently when scan and cross-scan were made at the so-called magic angles of 70 and 110 degrees, giving coverage over a field similar to a stretched hexagon.
   - The chop-nod point-source: Used PACS chopper and telescope nodding to move the target on the detector array defined in a predetermined pattern giving multiple positive and negative images that were combined. Early in the science mission it was found that the mini scanmap mode, although less efficient in terms of on-source time, was more sensitive, hence very few observations were obtained in this mode.
   - SPIRE PACS Parallel Mode: Was designed only for observing fixed targets and could not be defined for SSO observations, although many SSOs were observed serendipitously during mapping programmes in this mode. As the name indicates SPIRE and PACS were both scanning simultaneously, with PACS observing at 160 μm plus either 70 or 100 μm, while SPIRE scanned in its three photometric bands, giving simultaneous, wide area coverage in five filters. SPIRE PACS Parallel Mode was considered the fourth instrument of Herschel although, due to the fast scan speeds, sensitivity was quite low at 70 μm, thus PACS was considered to be an add-on, with SPIRE the prime instrument in this observing mode.
2. Line spectroscopy: A limited number of defined central wavelengths could be covered with a pre-determined spectral range at moderate to high spectral resolution. This mode was designed for observing individual lines in the spectrum.
3. Range spectroscopy: A spectral range could be requested to give wider wavelength coverage at intermediate resolution. This mode was intended for observing the Spectral Energy Distribution (SED) over part or the whole of the PACS wavelength range.

SPIRE

1. SPIRE photometer: Could be used in three different sub-modes:
   - Small Map Photometry: Was used for sources or areas smaller than 4 × 4 arc-minutes.
   - Large area of extended source mapping: Was used for sources or areas larger than 4 arc-minutes in diameter, the map was made by scanning with the telescope in one or two scanning angles.
   - SPIRE PACS Parallel Mode: Same observation mode as seen above in the PACS AOT, designed to map large areas of sky with high efficiency. In SPIRE PACS Parallel Mode the prime instrument was considered to be SPIRE, as the speed of scan meant that the PACS observations had rather shallow depth.
2. SPIRE spectrometer: The spectrometer was used to take spectra with different spectral resolutions. The spectra could be measures in single pointing (pixels within the FoV) or in large maps (made by moving the telescope in a raster).

HIFI

1. Single Point: Point source spectrophotometry, was used for observing a target at a single position on the sky in any one of fourteen sub-bands.
2. Mapping: Used for covering extended regions to produce spectral maps.
3. Spectral Scanning: The user could select the mixer band with which a body was observed at a single position on the sky over a continuous range of frequencies. This mode could be used to scan the spectrum of a target at intermediate to very high resolution over the full range of wavelengths covered by HIFI.

2.4 Herschel Data Products

Herschel has a wide variety of data products which are described in the *Herschel Product Definition Document* [1]. These are summarised bellow.

Most, but not all, of the Herschel data products were generated automatically by systematic pipeline processing at the Herschel Science Centre (HSC), available through the Herschel Science Archive (HSA) labelled with the version of the SPG (Standard Product Generation) software used for their production.

Herschel data products consist of:

- Observational products, containing scientific data from the Herschel observations sorted regarding the level of their processing:

  - Level-0 data products: raw telemetry data measure by the instrument.

  - Level-1 data products: detector readouts calibrated and converted to physical units.

  - Level-2 data products: further processed data so that they can be scientifically analysed.

  - Level-2.5 data products: improved with respect to those of level-2: these are different depending on the instrument and the AOT.

- Level-3 data products: mostly combinations and mosaics only available for PACS and SPIRE.

- Standalone Browse Products, such as postcards [4], for quick look purposes and not necessarily science ready products.

- Auxiliary products, comprise all the non-science spacecraft data necessary directly or indirectly in the processing and analysis of the scientific data.
- Calibration products, consist of the parameters that define the behaviour of the satellite and the instruments.
- Quality control products, assemble a summary of the information necessary to assess the technical quality of the observations and products generated providing a global quality assessment.
- User Provided Data Products (UPDPs), interactively reduced data provided by scientists to the HSC made available after validations.
- Highly Processed Data Products (HPDPs), improved products provided by experts in the ground segment to the HSC and stored in the HSA.
- Ancillary Data Products (ADPs), consisted of data generated in the course of different phases of the Herschel mission which are not necessarily linked to a particular observation.

2.5 Herschel Interactive Processing Environment

HIPE is a free, open software, built to be a platform-independent. It is based on Java and allows scripting programming in Jython (implementation of Python programming language integrated with the Java platform), it works in Linux, Windows and Mac.

HIPE is a software created for the purpose of facilitating to the scientific community the use of Herschel data products (e.g. to reduce the Herschel data interactively from level-0, -1 or -2 products and/or to perform scientific analysis on them). HIPE has direct access to HSA and is able to retrieve the data from the archive using the HSA user interface. The software has calibration data, useful user-developed routines, both in graphical user interface (GUI) form, or in console-batch mode. It contains the same pipeline scripts and tasks as the SPG as well as documentation. Astronomers can develop and integrate their processing algorithms in the system as well as visualise and manipulate images, spectral and spectral cube data [2], [3].

3 Catalogue Description

Four steps were performed in the creation of the Herschel Catalogue of Solar System Object Observations:

1. Compilation of the Herschel Catalogue of Solar System Object Observations.
2. Organization of the information in order to facilitate accessibility and retrieval.
3. Completion of the missing information in the catalogue.
4. Catalogue dissemination and preserving it as part of the Herschel Legacy Archive.

In this section, the first and second steps are described.

3.1 Compilation of the Observations

The HCSSOO is compiled from all Herschel's science observations of the Solar System: a total of 1692 AORs, excluding those observations with the quality control state of "failed". These cover 170 Solar System Objects. These observations were obtained via multiple observing programs [12] and [11] ranging from single observations to large programmes of several hundred hours duration, covering a total of 853.1h of observing time, of which 457h were dedicated to photometry and 396 hours to spectroscopy. The data on Herschel's observations of SSOs was extracted from the Herschel Observing Log [13]. However, in order to give context to the catalogue, other information of interest was compiled:this will be detailed in the breakdown of the contents of each column of the catalogue in the section on "Organization of the Information". Information was compiled from 63 publications using Herschel SSO data, which are listed in Appendix B of this Explanatory Supplement.

The 170 Solar System bodies that Herschel observed consist of:

1. Major planets: 5

   Mars, Jupiter, Saturn, Uranus and Neptune.

2. Dwarf planets: 5

   Pluto, Eris, Ceres, Makemake and Haumea.

3. Satellites: 6

   Ganymede and Callisto of Jupiter; Enceladus, Titan and Phoebe of Saturn; Sycorax of Uranus.

4. Comets:14, of which

   - Short period comets:6

     67P/Churyumov-Gerasimenko, 103P/Hartley 2, 29P/Schwassmann-Wachmann 1, 9P/Tempel 1, 10P/Tempel 2 and 45P/Honda-Mrkos-Pajdusakova.

   - Long period comets: 8

     Hale-Bopp (C/1995 O1), Christensen (C/2006 W3), Garradd (C/2009 P1), C/2010 X1/Elenin, PANSTARRS (C/2011 L4), ISON (C/2012 S1), PANSTARRS (P/2012 T1) and Siding Spring (C/2013 A1).

5. Transitional Objects (asteroids with occasional cometary activity): 3

   2060 Chiron, 60558 Echeclus and 118401 LINEAR.

6. Minor planets: 137, of which:

   - Near Earth Asteroids: 6

     101955(1999 RQ36)/Bennu, 2005 YU55, 175706(1996 FG3) and 162173 (1999 JU3)/Ryugu from Apollo group; 99942 Apophis from Aten group; 433 Eros from the Amor group.

   - Main Belt Asteroids: 5

     253 Mathilde, 65 Cybele, 21 Lutetia, 2867 Steins and 24 Themis.

   - Centaurs: 22, see Table 1.

8405 Asbolus	145486 (2005 UJ438)
52872 Okyrhoe	250112 (2002 KY14)
55576 Amycus	2005 RO43
54598 Bienor	2006 SX368
65489 Ceto	2007 RW10
10199 Chariklo	2008 FC76
10370 Hylonome	2012 DR30
73480 (2002 PN34)	2013 AZ60
95626 (2002 GZ32)	5145 Pholus
120061 (2003 CO1)	32532 Thereus
136204 (2003 WL7)	42355 Typhon

Table 1: Minor planets - Centaurs.

   - Trans-Neptunian Objects/Centaurs: 3

     78799 (2002 XW93) and 120181 (2003 UR292) classical TNOs; 127546 (2002 XU93) Detached Object.

   - TNOs: 101 (41 classicals, 4 Detached Objects, 42 resonants and among them 26 Plutinos and 4 Twotinos, 11 Scattered-Disk Objects and 3 classified as other TNOs for not having enough orbital information to give a definitive class). See Tables 2, 3 and 4.

66652 Borasisi	2003 WU188	55637 (2002 UX25)
79360 (1997 CS29)	2001 XR254	2001 RZ143
19521 Chaos	2001 QY297	55636 (2002 TX300)
20000 Varuna	2003 QA91	35671 (1998 SN165)
148780 Altjira	2004 NT33	55565 (2002 AW197)
202421 (2005 UQ513)	50000 Quaoar	86177 (1999 RY215)
2001 QS322	135182 (2001 QT322)	90568 (2004 GV9)
2005 EF298	138537 (2000 OK67)	119951 (2002 KX14)
120347 (2004 SB60)/Salacia	145452 (2005 RN43)	120178 (2003 OP32)
88611 Teharonhiawako	174567 (2003 MW12)	2003 UZ117
2004 PT107	145453 (2005 RR43)	230965 (2004 XA192)
2001 KA77	2001 QD298	2002 GV31
2002 GH32	2002 KW14	2002 MS4
2003 QW90	2003 GH55	

Table 2: Minor planets - TNOs - Classical.

Body	Classification	Body	Classification
38628 Huya	Plutino	2003 UT292	Plutino
28978 Ixion	Plutino	2003 WU172	Plutino
139775 (2001 QG298)	Plutino	2006 HJ123	Plutino
208996 (2003 AZ84)	Plutino	2003 UZ413	Plutino
47171 (1999 TC36)	Plutino	90482 Orcus	Plutino
15820 (1994 TB)	Plutino	119979 (2002 WC19)	Twotino
15875 (1996 TP66)	Plutino	2003 FE128	Twotino
33340 (1998 VG44)	Plutino	26308 (1998 SM165)	Twotino
47932 (2000 GN171)	Plutino	2005 RS43	Twotino
55638 (2002 VE95)	Plutino	26375 (1999 DE9)	Resonant 2:5
84719 (2002 VR128)	Plutino	84522 (2002 TC302)	Resonant 2:5
84922 (2003 VS2)	Plutino	143707 (2003 UY117)	Resonant 2:5
120216 (2004 EW95)	Plutino	2002 GP32	Resonant 2:5
120348 (2004 TY364)	Plutino	26181 (1996 GQ21)	Resonant 2:11
133067 (2003 FB128)	Plutino	126154 (2001 YH140)	Resonant 3:5
144897 (2004 UX10)	Plutino	82075 (2000 YW134)	Resonant 3:8
175113 (2004 PF115)	Plutino	225088 (2007 OR10)	Resonant 3:10
2001 KD77	Plutino	42301 (2001 UR163)	Resonant 4:9
2001 QF298	Plutino	2000 CN105	Resonant 5:9
2002 VU130	Plutino	2001 QX322	Resonant / DO
2002 XV93	Plutino	119878 (2002 CY224)	Resonant / SDO

Table 3: Minor planets - TNOs - Resonants.

Body	Classification	Body	Classification
15874 (1996 TL66)	SDO	229762 (2007 UK126)	SDO
40314 (1999 KR16)	SDO	48639 (1995 TL8)	SDO
44594 (1999 OX3)	SDO	120132 (2003 FY128)	DO
82155 (2001 FZ173)	SDO	145480 (2005 TB190)	DO
82158 (2001 FP185)	SDO	2004 PG115	DO
145451 (2005 RM43)	SDO	90377 Sedna	DO
2005 QU182	SDO	19308 (1996 TO66)	Other TNO
2007 OC10	SDO	24835 (1995 SM55)	Other TNO
2010 EK139	SDO	1999 CD158	Other TNO

Table 4: Minor planets - Remaining TNOs.

A better way of obtaining a global vision of the 170 SSO that were observed in the 1692 science observations is obtained by looking at the graphics below, Figures 3, 4 and 5.

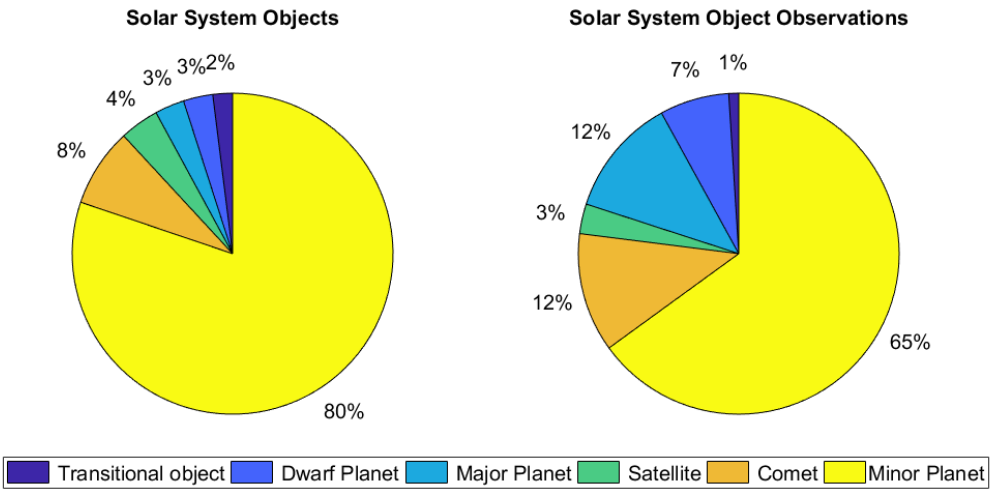

Figure 3: Percentage of Solar System Objects and their observations. Although Minor Planets (including TNOs) make up 80% of observed SSOs, they make up only 65% of the AORs. In contrast, Major Planets make up just 3% of the SSO targets observed, but form 12% of the AORs.

In Figure 3, the graphic on the left shows the classification of the 170 SSO and the percentage of each of the classes over the total. The graphic on the right shows the classification of the 1692 Solar System Object Observations and the percentage of their presence in the catalogue. From the graphics, some facts about the observations can be extracted. For instance, there is a larger number of satellites observed than of major planets, but the planets have 4 times more dedicated observations than the satellites, therefore the planets can be better analysed than the satellites. Minor planets, both classical Main Belt objects, Near Earth Objects and the TNOs and related objects, have the biggest presence in the catalogue, both in number of objects and in observations and therefore this target classification will be analysed in more detail than the others.

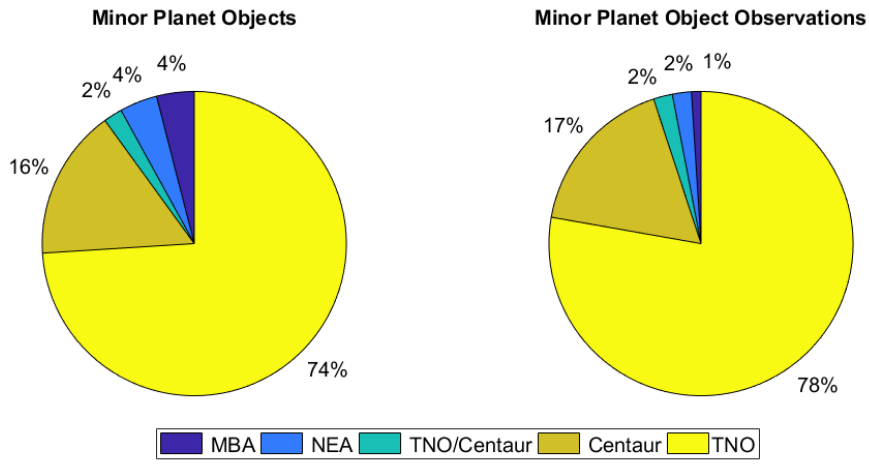

Figure 4: Percentage of minor planets objects and their observations.

In Figure 4, the graphic on the left shows the classification of the 137 objects classified as Minor Planet and the percentage of each of the classes over the total of minor planets, the graphic on the right shows the classification of the 1101 minor planet observations and the percentage of their presence among them. In this graphic, we can see that the observations of TNOs had an important role in the catalogue, since they are the most abundant and the most observed class in the HCSSOO and because of this, TNOs will be analysed in more detail. The reason why TNOs are so abundant in Herschel's observations is because by operating in far-infrared, Herschel could observe this very cold objects in ways that they were never observed before: Measurements of thermal emission, which peaks at FIR wavelengths, offer the best means available to determine the physical properties, the sensitivity and wavelength coverage of Herschel permitted profound advances in the field.

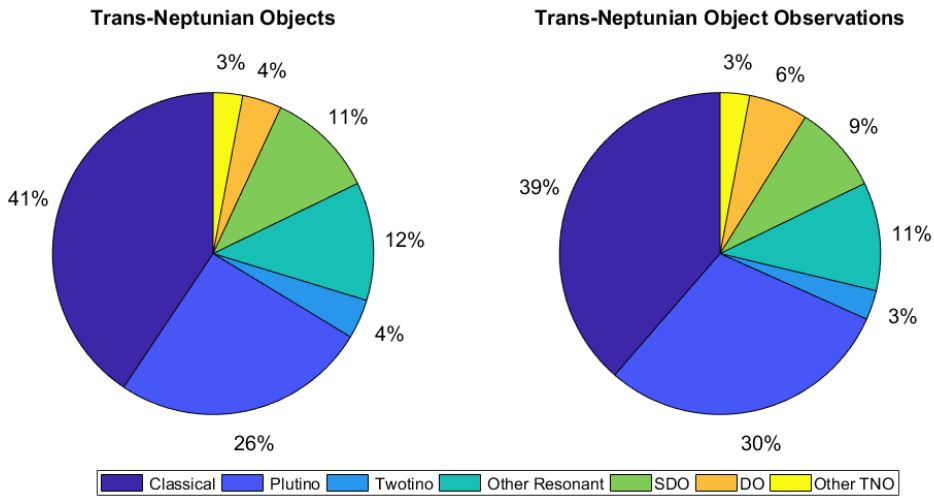

Figure 5: Percentage of TNOs and their observations.

Figure 5 shows the classification of the 101 Trans-Neptunian Objects and the percentage of each of the classes over the total of TNOs of the sample. The graphic on the right shows the classification of the 952 TNO observations and the percentage of their presence

among them. With this graphic we can see that the classicals and the Plutinos are the most abundant and observed objects in the catalogue.

3.2 Organization of the Information

In order to provide a catalogue of Solar System Object Observations that is as complete as possible, information was extracted not only from the Herschel Observing Log [13] but also from other sources and publications, see Appendix B. In this subsection the columns of the catalogue will be explained in detail and for that purpose we have to divide them into the following three parts.

3.2.1 Classification of the Targets

In this part, the columns included, see Tables 5 and 6, are the ones that help identifying and classifying the target. These columns contain the following information:

NAIF ID	IAU nomenclature	Target	Alternative names

Table 5: Column information: classification of the targets - part 1.

First Classif.	Dynamical Classif.	Second Dynamical Classif.	Classif. Comm.

Table 6: Column information: classification of the targets - part 2.

- **NAIF ID**: The NAIF integer ID codes are unique integers assigned to each body in the solar system [21].
- **IAU Nomenclature**: The International Astronomical Union Committees and Working Groups have certified the names of astronomical objects and surface features since 1919: this is known as IAU nomenclature [18].
- **Target**: In this column, we give the name of the body observed, as recorded in the observation log of the Herschel mission [13].
- **Alternative names**: Alternative names have been listed. These may be the previous, provisional designation of the bodies, or other designations that can be find in scientific publications, see Appendix B for an index of all the publications used in the catalogue [17].
- **First Classification**: Classification of the solar system bodies into major planets, dwarf planets, satellites, minor planets, transitional objects and comets [21], [18], [17].
- **Dynamical Classification**: The bodies are classified according to their dynamic behaviour (e.g. orbit characteristic) into: Near Earth Asteroids, Main Belt Asteroids, Main Belt Comets, Centaurs, Trans-Neptunian Objects and TNOs/Centaurs. The information was obtained from [17], [19] and publications, see Appendix B.
- **Second Dynamical Classification**: A second classification was applied for the TNOs dividing them into: classicals, Plutinos, Twotinos, other resonants (e.g. Resonant 4:9, Resonant 3:5,...), Scattered Disk Objects and Detached Objects. The information was obtained from [17], [19] and publications, see Appendix B.

- **Classification Comment**: In this column we indicate an extra information on the body, if available, such as members of orbital groups and families (Amor, Apollo, Aten, Haumea, Cybele, Senoid), the type of cometary orbit (long/short period comet), if an asteroid has shown cometary activity, or if it forms part of a binary or multiple system body, as well as an indication of the existence of rings in the system.

3.2.2 Ancillary Information

In this part the columns, see Table 7 and 8, provide all the ancillary information for each SSOO and other relevant information of the observations excluding physical properties.

ObsID	OD	Start Time	Integration Time

Table 7: Column information: ancillary information - part 1.

Proposal	Mode	Instrument	S/P	WL

Table 8: Column information: ancillary information - part 2.

- **ObsID**: Corresponds to the identifier of the Herschel observation. The observation ID uniquely identifies an observation for all mission phases [14], [13].
- **OD**: The operational day of the mission to which the observation belongs to [14], [13].
- **Start time**: The starting time of the observation of the body in the following format: (yyyy-mm-dd hh:mm:ss) In UTC time system and fine time, which is defined as the atomic time (SI seconds) elapsed since the TAI epoch of 1 January 1958 UT2 [14], [13].
- **Integration time**: Duration of the observation in seconds [14], [13].
- **Proposal**: Proposal name for the observations of the body, or bodies, during Herschel's observing time (GT, OT and DDT). Guaranteed Time, Open Time and Director's Discretionary Time are explained at the end of section 2.1 of this Explanatory Supplement [14], [13].
- **Mode**: Observational mode used for the AOR. The Astronomical Observation Templates are described in section 2.3 of this Explanatory Supplement [14], [13].
- **Instrument**: Instrument employed, for the observation: HIFI, PACS, SPIRE [14], [13].
- **S/P**: In this column we indicate if the AOR executed was a spectroscometer (S), or a photometer (P) observation [14], [13].
- **WL(1/2/3)**: Indicates the wavelength, or wavelengths (in micrometres), that were used in the observation [14], [13].

3.2.3 Physical Circumstances

These columns, see Tables 9, 10, 11 and 12 provide information of the bodies' physical properties that were considered interesting for the future analysis.

Albedo	Positive_STD_Albedo	Negative_STD_Albedo	V-R	V-R_STD	B-V	B-V_STD

Table 9: Column information: physical circumstances - part 1.

Ra/Dec	Illumination	r	Delta	Phase (STO)	Temperature	Method Flux Obs

Table 10: Column information: physical circumstances - part 2.

Method Flux Comm.	WL	WL_Comm.	WL_Flux	WL_Flux_STD

Table 11: Column information: physical circumstances - part 3.

CC_WL_This Work	WL_This Work

Table 12: Column information: physical circumstances - part 4.

- **Albedo / Positive STD Albedo / Negative STD Albedo**: The Albedo is the fraction of the incident light reflected from the surface of a celestial body, expressed as the ratio of reflected light vs incident light. In this catalogue, we list the geometric albedo, which uses a flat Lambertian surface (surface which is uniformly bright from all viewing directions and reflects the entire incident light) for the calculations.

  When available, we give the values of the albedo expressed as a fraction from 0-1. In the following two columns, the positive and the negative STD, when available, are also indicated, see the publications in Appendix B [20], [24].

  When an albedo value is indicated, but its standard deviations is given as 0, the only value available is a lower limit: Real Albedo (unknown) > Value Albedo.

- **V-R / V-R STD**: is a colour index. This index is the difference between magnitudes, in this case V and R, with negative values indicating a blue colour and increasingly positive values a red colour. Where available, the V-R colour index is given and in the following column, its standard deviation. To consult the sources, see the publications in the Appendix B.

- **B-V / B-V STD**: is a colour index. Where available, the B-V colour index is given and in the following column, its standard deviation. To consult the sources, see the publications in the Appendix B.

- **Ra/Dec**: Astrometric Right Ascension and Declination of the target centre with respect to the Herschel Space Observatory position, measured in hours, minutes and seconds [HH MM SS.ff] and degrees, minutes and seconds [DD MM SS.f] respectively. Expressed with respect to the planetary ephemeris ICRF/J2000 equator and equinox. Measured at the midpoint of the integration using the target's ephemerides provided by *Horizons Web-Interface* [20].

- **Illumination**: Illuminated fraction seen by the observer, also known as phase, measured in %. Phase is the portion of the target object circular disk illuminated by the Sun as seen by the observer, with the observer the Herschel Space Observatory. Measured at the midpoint of the integration [20].
- **r**: Heliocentric range in AU. Measured at the midpoint of the integration [20].
- Δ: Range from the target centre to the observer in AU, the observer being the Herschel Space Observatory (i.e. the Herschelcentric distance). Measured at the midpoint of the integration [20].
- **Phase (STO)**: Angle measured in degrees between the Sun-target-observer. This is slightly different to the phase angle, as it includes stellar aberration in both vectors.
- **Temperature**: Theoretical greybody temperature of the body measured in Kelvin [K]. Calculated in this work. The calculation will be explained in the next section "Completion of Missing Information: Photometric Calculation".
- **Method Flux Obs**: Shows the method used in the calculation of the fluxes (e.g. aperture photometry, polarimetry), see the publications in Appendix B.
- **Method Flux Comm.**: Gives more information about the method used in the calculation of the fluxes, when available (e.g. wavelength followed by the aperture radius, the inner radius of the sky annulus and the outer radius of the sky annulus in arc-seconds), see the publications in Appendix B.
- **WL_(1/2/3)**: This column indicates the wavelength or wavelengths in micrometres at which the flux was measured. For PACS photometry: WL_1 = 70, WL_2 = 100, WL_3= 160). For SPIRE photometry: (WL_1 = 250, WL_2 = 350, WL_3 = 500). For the special case of HIFI spectroscopy: (WL_1 = 530.7).
- **WL_(1/2/3)_Comm.**: A comment that indicates if the flux has been averaged using all the body's flux values for that wavelength or not. The flux can only be averaged between observations of consecutive observations with a difference no bigger than 20 arcsec between the position of the body in this consecutive observations. A 1 indicates that the flux has been averaged, 0 indicates that the flux has not been averaged. See the publications in Appendix B.
- **WL_(1/2/3)_Flux**: Monochromatic flux densities measured in milliJansky (mJy). See the publications in Appendix B [24].
- **WL_(1/2/3)_Flux_STD**: This column shows the standard deviation of the measured flux in mJy. See publications in the Appendix B, [24].

  If there is a value in the Flux column but the Flux STD has the indication of Not Available (NA) means that that flux is unknown and the only information available is this upper limit: Real Flux (unknown) $<$ Value Flux (the information that we have).
- **CC_WL_(1/2/3)_ThisWork**: This column indicates whether or not the fluxes "in band" extracted from publications, which were not colour corrected as published, have been corrected in this catalogue. 1 indicates that the flux was colour corrected in this work using flux in band values from publication. See the publications in Appendix B. A blank cell indicates that the flux "in band" from the publications was already colour corrected and no further calculations was performed in this work.

- **WL_(1/2/3)_ThisWork**: This column indicates whether or not the values of the flux and flux standard deviation have been calculated in this work (1 for yes, 0 for no).

3.2.4 Example

An example of the columns of the catalogue and the information of an observation can be seen in the following Tables 13, 14, 15, 16, 17, 18, 19, 20, 21, 22 and 23:

NAIF ID	IAU Nomenclature	Target	Alternative Name
2038628	38628	38628 Huya	Huya / 2000 EB173

Table 13: Example: classification of the targets - part 1.

First Classif.	Dynamical Classif.	Second Dynamical Classif.	Classif. Comm.
Minor Planet	TNO	Plutino	Binary 213

Table 14: Example: classification of the targets - part 2.

ObsID	OD	Start Time	Integration Time
1342202873	455	2010-08-11 19:01:34	568

Table 15: Example: ancillary information - part 1.

Proposal	Mode	Instrument	S/P
KPOT_thmuelle_1	PACSPhoto	PACS	P

Table 16: Example: ancillary information - part 2.

WL1	WL2	WL3
70	160	NA

Table 17: Example: ancillary information - part 3.

Albedo	Positive_STD_Albedo	Negative_STD_Albedo	V-R	V-R_STD	B-V	B-V_STD
0.083	0.004	0.004	0.57	0.09	0.95	0.05

Table 18: Example: physical circumstances - part 1.

Ra/Dec	Illumination	r	Delta	Phase (STO)	Temperature
14 54 18.00 -03 20 37.6	99.969	28.665	28.761	2.0294	70.66

Table 19: Example: physical circumstances - part 2.

Method Flux Obs	Method Flux Comm.
Aperture photometry	70(5.2”-6.5”NA”NA”)160(12”-15”NA”NA”)

Table 20: Example: physical circumstances - part 3.

WL_1	WL_1_Comm.	WL_1_Flux	WL_1_Flux_STD	CC_WL_1_ThisWork	WL_1_This Work
70	1	47.6	1.7	NA	0

Table 21: Example: physical circumstances - part 4.

WL_2	WL_2_Comm.	WL_2_Flux	WL_2_Flux_STD	CC_WL_2_This Work	WL_2_This Work
NA	NA	NA	NA	NA	NA

Table 22: Example: physical circumstances - part 5.

WL_3	WL3_Comm.	WL3_Flux	WL3_Flux_STD	CC_WL3_This Work	WL3_This Work
160	1	25.6	2.4	NA	0

Table 23: Example: physical circumstances - part 6.

3.3 Listing of column headings used

In the following list appear in order the names of the column headings used in the catalogue. The description of the columns can be found in the above subsections.

1. **ObsID**
2. **NAIF ID**
3. **IAU Nomenclature**
4. **Target**
5. **Alternative names**
6. **First Classif.**
7. **Dynamical Classif.**
8. **Second Dynamical Classif.**
9. **Classif. Comm.**
10. **OD**
11. **Start Time**
12. **Integration time**
13. **Proposal**
14. **Mode**
15. **Instrument**

16. **S/P**
17. **WL1**
18. **WL2**
19. **WL3**
20. **Albedo**
21. **Positive STD Albedo**
22. **Negative STD Albedo**
23. **V-R**
24. **V-R STD**
25. **B-V**
26. **B-V STD**
27. **Ra/Dec**
28. **Illumination**
29. **r**
30. Δ
31. **Phase (STO)**
32. **Method Flux Obs**
33. **Method Flux Comm.**
34. **WL_1**
35. **WL_1_Comm.**
36. **WL_1_Flux**
37. **WL_1_Flux_STD**
38. **CC_WL_1_ThisWork**
39. **WL_1_ThisWork**
40. **WL_2**
41. **WL_2_Comm.**
42. **WL_2_Flux**
43. **WL_2_Flux_STD**
44. **CC_WL_21_ThisWork**
45. **WL_2_ThisWork**
46. **WL_3**
47. **WL_3_Comm.**
48. **WL_3_Flux**

49. **WL_3_Flux_STD**
50. **CC_WL_3_ThisWork**
51. **WL_3_ThisWork**
52. **Temperature**

4 Completion of Missing Information: Photometric Calculation

In the previous section, we have shown how the scientifically interesting information in the columns has been structured into three parts. The physical circumstances part is the most interesting one because it provides relevant physical characteristics of the objects that can be used for analysis and studies.

Some of the bodies do not have information on all the physical characteristics that are listed in the physical circumstances columns: these are indicated with a "Not Available" note. The third step of the creation of the catalogue consisted of the completion of missing information. Since Herschel performed photometric observations, it was considered of the greatest interest to complete all the possible photometry measurements and finalize this task for the observed Solar System objects.

We attempted to complete the missing fluxes from PACS photometry as they present 76% of Herschel's Solar System observations. HIPE, v15.0.0 was used to extract photometry, as explained in the section 2.5.

The PACS photometry AOTs, described in the section 2.3, could be of two types: scan maps and mini scan map/point source and chop-nod point-source. There are, in total, 1287 PACS photometry observations, of which 1277 are scan map and mini scan map/point source and 10 are chop-nod point-source.

The chop-nod mode was an observing mode used only in the early stages of routine observing. Only ten observations were taken using this mode at the beginning of the operational phase. Due to the known difficulties with calibration of this mode and its rapid deprecation, we preferred not perform photometry on observations carried out using this observational mode. The ObsIDs involved are:

- 1342183654
- 1342183655
- 1342187367
- 1342187366
- 1342187114
- 1342187113
- 1342187073
- 1342187074
- 1342187062
- 1342187054

4.1 Scan Map and Mini Scan Map/Point Source

To perform photometry on scan map and mini scan map/point source AOT, their observational products, processed by the SPG, were used. Level-2.5 data products (see section 2.4 for Herschel Data Products) were chosen over level-2 data products, when available as these are the highest level of science ready products.

Level-2 data products are maps generated by detector readouts from level-1, projected on to a sky grid using the High-Pass Filtering (HPF) pipeline to remove the 1/f noise from the observations. 1/f noise is also called pink noise, is very common in nature and it has the following spectral form:

$$S(f) = \frac{1}{f^{\alpha}} \tag{1}$$

In Equation 1, f represents the frequency and α ranges between 0 and 3, when $\alpha = 1$, is the general case for pink noise [82].

Level 2 data maps are denominated as Herschel PACS Photometer PhotProject MAP Blue/Red (HPPPMB, or HPPPMR) depending on the observing wavelength (blue for 70 and 100 μm and red for 160 μm). The units of the map are in Jy/(map pixel).

Level-2.5 data products are maps that have been created for observations that had the AOT of using scan and cross-scan. For the level-2.5 product, these two scans have been combined into a single map, eliminating the majority of the systematic noise in an individual scanmap thus, although Level 2 products can be used to generate photometry, Level 2.5 are preferred if they are available and give a superior quality of science.

There are different level-2.5 science ready maps. The most common ones used are Unimap [25], [85], which uses the Generalised Least Squares approach with the pixel noise compensation to remove the low frequency noise (1/f) and JScanam, [51] which uses the Scanamorphos algorithm [90], to remove the 1/f noise. Both of them are flux calibrated in units of Jy/(map pixel).

For the photometric calculation, level-2.5 Unimap maps were used. The reason for this decision is that, according to the publication *PACS Map-making Tools: Analysis and Benchmarking* [78], Unimap, although very similar to JScanam provides less noisy measurements when observing faint point source photometry (0.001 - 0.1 Jy) and since most of our objects are TNOs, we can expect them to have faint fluxes and thus more suited to the Unimap product.

The Unimap maps are denominated Herschel PACS Photometer UNIMAP Blue/Red (HPPUNIMAPB or HPPUNIMAPR) depending on the observing wavelength (blue for 70 and 100 μm and red for 160 μm).

From the 1277 observations in scan map and mini scan map/point source observation mode there are 1240 observations processed up to level-2.5 and only 37 observations that could only be processed up to level-2. In both cases the maps were introduced into the following pipeline for performing the photometric calculation.

4.1.1 Photometric Calculation Pipeline

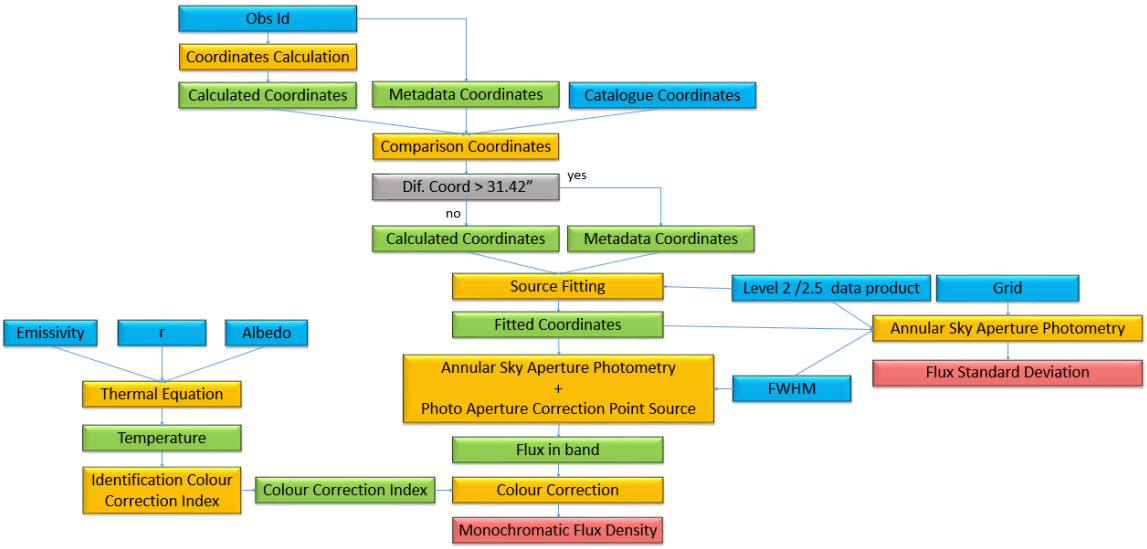

Figure 6: Photometric calculation pipeline.

The pipeline represented in Figure 6 shows the inputs (in blue), steps (in yellow), conditions (in grey), intermediate outputs (in green) and final outputs (in pink) from the start to the end of the photometric calculation. This pipeline, which was used for all Scan Map and Mini Scan Map/Point Source observations, is explained in this section.

1. Coordinates Calculation

   When performing photometric calculations, especially on faint bodies, it is very important to have precise target coordinates. These coordinates, as explained, were measured at the midpoint of the integration, using the target's ephemerides provided by JPL Horizons System Web-Interface [20].

   For diverse reasons, some of the observations were offset from the target and therefore even if the coordinates of the target are good, the named target does not appear in the map. As an example, see Figure 7, where Saturn was observed, but with an offset to study extended material in the ring system, hence the planet itself is not in the map. Similarly, the ephemeris used to plan the Herschel observation could, in some cases, have errors as large as 30 arcseconds hence, if there were several sources close to the centre of the map, it was sometimes not obvious which was the intended target.

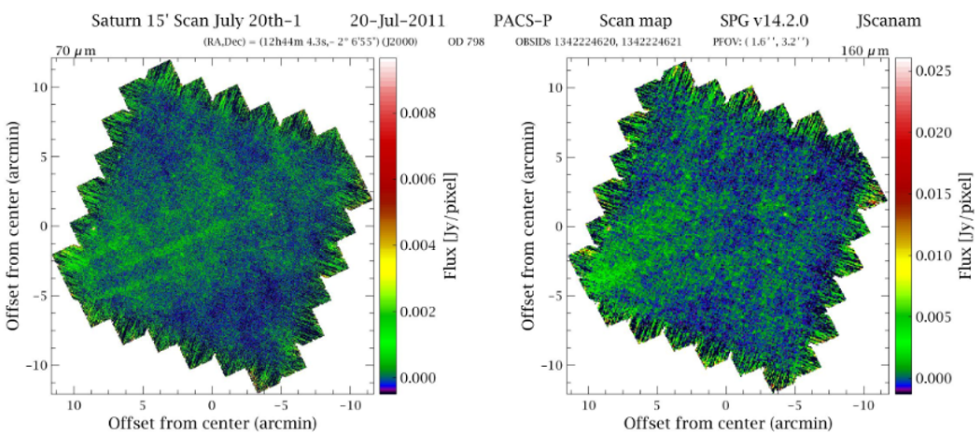

Figure 7: Example of observed body outside the map due to a programmed offset in target coordinates.

Observation: Saturn 15'/40' Scan July 20th-1/2 - ObsIDs: 1342224621 / 1342224623.

To resolve this issue, HIPE was used to re-calculate the coordinates of the bodies. Each observation has a unique observation ID that, when introduced in HIPE, allows us to obtain information from the meta-data of the target, such as NAIF ID and the Horizons ephemeris, which were used to calculate the coordinates of the object in the corresponding moving target reference frame, taking advantage of the latest ephemeris available, which may be much more accurate than the one used originally to schedule the observations. In the cases in which the body does not appear in the map, there will be no NAIF ID information and the observation can be marked and deleted from the list.

Another piece of information that was extracted from the meta-data was the meta-data coordinates, which indicate the centre of the FoV of the map where the telescope thought that the target would be: normally the target observed is situated in or close to the centre of the map but, even with a perfect ephemeris available at the time of scheduling, the telescope had its own, random pointing error, although this reduced progressively through the mission, hence a 10 arcsecond pointing error could occur statistically, even in a perfectly executed observation of a target with perfectly known coordinates [92].

2. Comparison of Coordinates and Difference between Coordinates

   The three sets of coordinates available: calculated coordinates, meta-data coordinates and the catalogue coordinates were compared.

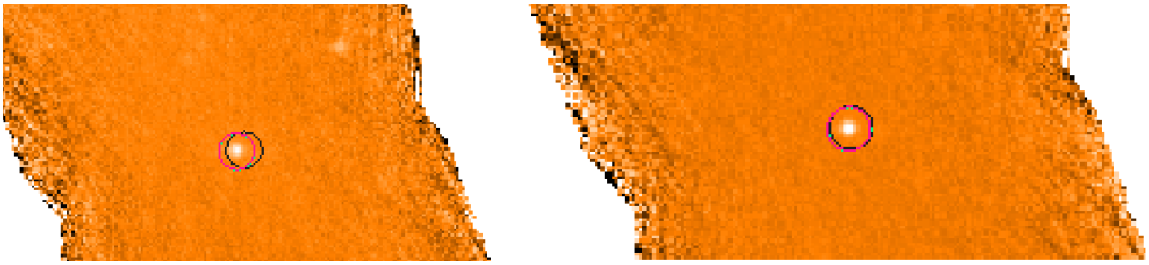

Figure 8: Comparison between coordinates - similar results.
Observation: 10199 Chariklo - ObsIDs: 1342202373 / 1342202374 - HPPUNIMAPB / HPPUNIMAPB.

In most of the cases, the three sets of coordinates will be very similar and the identification of the target will be a trivial exercise, for example, see Image 8. The black ring has as centre the meta-data coordinates, the green ring has as centre the calculated coordinates and the pink ring has as centre the catalogue coordinates. All the rings have 5" radii.

But in other cases, see Figures 9 and 10, the coordinate centres differ. In Figure 9, the coordinates from the catalogue and the calculated ones provide a better result than the coordinates from the meta-data, this is not a surprise since the meta-data coordinates are just the centre of the field of view: in other words, where it was believed that the object would be when it was scheduled for observation. In Figure 10 the coordinates from the meta-data have a better target centring than the others, but there is no ambiguity in source identification.

Recapitulating: there are three possible sets of coordinates to use. The catalogue coordinates, which are similar to the calculated coordinates, but if choosing which to use between those two, the calculated coordinates should be used, since they discard the bodies which are not present in the map, as seen in the first point of the pipeline. Between the calculated coordinates and the meta-data, the calculated coordinates should be chosen, since the meta-data coordinates are expected to be the least accurate, as they use old ephemeris information. What though, should we do with a case such as Figure 10?

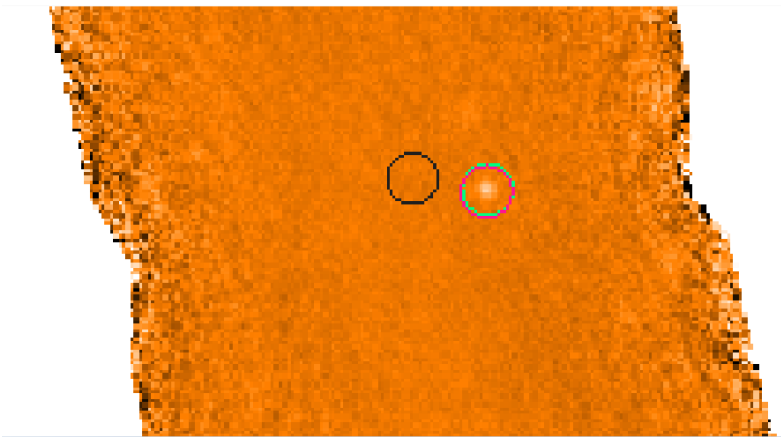

Figure 9: Comparison between coordinates - different results 1.
Observation: 2013 AZ60-1 - ObsID: 1342268990 - HPPUNIMAPB.

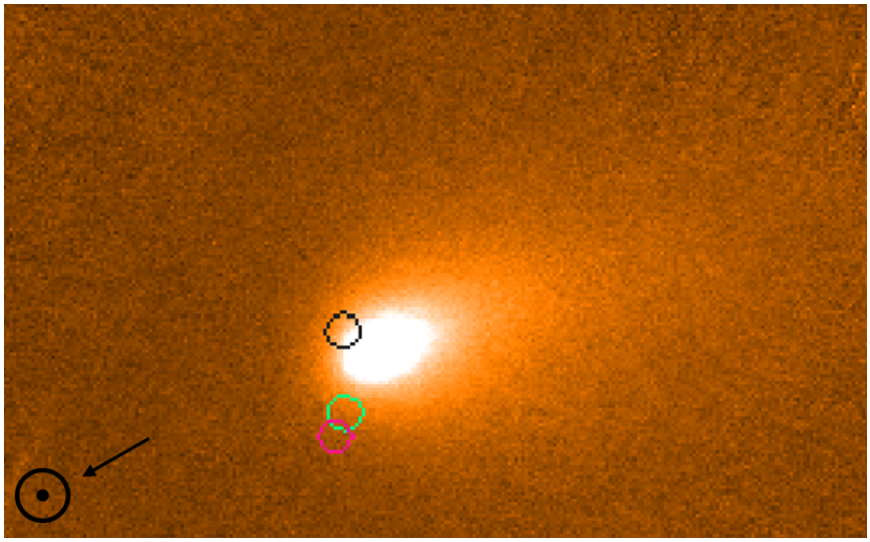

Figure 10: Comparison between coordinates - different results 2. The arrow indicates the projected direction of the comet towards the Sun. Observation: 103P/Hartley 2 - ObsID: 1342209385 - HPPUNIMAPB.

A study of the differences between the right ascensions and the declinations of the meta-data and the calculated coordinates was carried out, see Table 24, where σ is the standard deviation and μ the arithmetic mean. From the table we can see that both mean values are close to zero arc-seconds, so it can be deduced that the two sets of coordinates are quite similar. Regarding the Right Ascension difference, the standard deviation is quite small, so it indicates that there are no big discrepancies between the two sets of coordinates, but for the declination, the standard deviation has a value of approximately 15 arc-second, which indicates that some sets of coordinates are quite different to others. Since an aperture radius around the centre of the target will be larger than $2\times\sigma$ of the right ascension, the set of coordinates for which the differences were bigger than $2\times\sigma$ in the declination = 31.42", were analysed. There were 8 observations over this threshold. All of them had similar characteristics to Figure 10, where the meta-data had a better centring than the calculated coordinates, therefore for these 8 observations only, the coordinates used are the meta-data coordinates.

	Ra_Calculated - Ra_Meta-Data	Dec_Calculated - Dec_Meta-Data
σ	01.21"	15.71"
μ	00.24"	-02.15"

Table 24: Comparison between calculated and meta-data coordinates.

3. Source Fitting

   The coordinates for the observations, together with the level-2 and level-2.5 maps, were used as the initial position to perform a source fitting to calculate the fitted coordinates of the body.

   The HIPE source fitting task [15] determines the centre of a body by fitting a 2-D circular Gaussian to the source in an indicated region. Using the observations' coordinates as the starting point, a rectangular box for the source fitting task to

search in was created. The centre of the fitted Gaussian were then the adopted coordinates of the object.

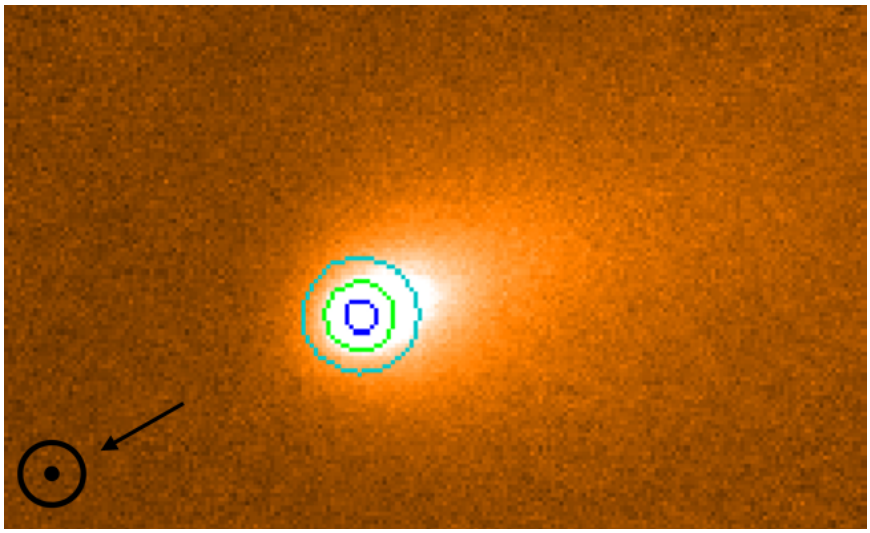

Figure 11: Source fitting example for an extended source. The arrow indicates the projected direction of the comet towards the Sun. Observation: 103P/Hartley 2 - ObsID: 1342209385 - HPPUNIMAPB.

In Figure 11 we can seen the same map as in Figure 10, but after the source fitting task was performed. The fitted coordinates, output of the source fitting task, are perfectly in the centre of the target. The three rings, from smallest to largest, correspond respectively to the aperture radius and the inner and outer radii of the sky annulus.

4. Annular Sky Aperture Photometry and Photo Aperture Correction Point Source

   In order to perform aperture photometry, the level-2 or level-2.5 maps, the fitted coordinates and the sizes of the radii to be used were needed as input. The chosen size for an aperture radius that is recommended for Herschel photometry is usually 1.4× FWHM, [89]. The inner and outer radii of the sky annulus are normally a scalar multiple of this value, typically 3× FWHM and 5× FWHM were chosen for the inner and outer radii of the sky annulus respectively.

   The FWHM of PACS was obtained from the *Quick-Start Guide to Herschel-PACS the Photometer* [38]. The FWHM values for the most common photometric observing modes are the following ones:

Band	Blue	Green	Red
Wavelength	70 μm	100 μm	160 μm
Beam FWHM ["]	5.6	6.8	10.7

Table 25: Beam FWHM for the most common mode of PACS.

Aperture photometry was performed using the "Annular Sky Aperture Photometry" task [16] and the fluxes were aperture corrected with the factors calculated for PACS using the "Photo Aperture Correction Point Source" task [16]. The results obtained were the flux in band. An example of aperture photometry can be seen in Figure 12.

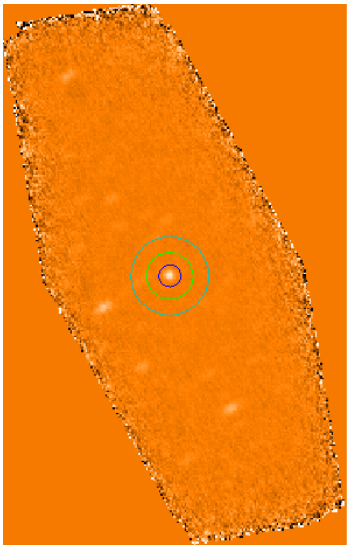

Figure 12: Aperture photometry example for a point source.
Observation: 208996 (2003 AZ84) - ObsID: 1342205152 - HPPPMAPB.

5. Thermal Equation

The goal of the photometric computation is to obtain the monochromatic flux densities. To do so, the flux in band had to be colour corrected and, in order to determine the colour correction indexes, the temperature of the body must be known, of at least, approximated.

The thermal equation applied in the publication of *"TNOs are cool: A survey of the trans-Neptunian region. V. Physical characterization of 18 Plutinos using Herschel-PACS observations*", Eq. 3 [69] was used for computing the temperature of the objects.

$$T_{SS} = \left[\frac{(1-A)S_{\odot}}{\varepsilon\sigma\eta r^2}\right]^{\frac{1}{4}} \tag{2}$$

In Equation 2, the temperature in Kelvin for a Solar System object is calculated.

"A" corresponds to the albedo of the object, in the cases where the albedo was not known the value 0.10 was used, since normally TNOs have an albedo lower than 10% and the dust or grain coma albedo would also be around 10% for an active comet.

$S_{\odot}$ is the solar constant which is defined as the total irradiance of the sun at the mean orbital distance of the Earth, it has a value of 1368Wm^{-2} [94].

ε refers to the emissivity, which is the effectiveness of a surface in emitting energy as thermal radiation, the values ranges from 0-1, with $\varepsilon = 1$ the value for a perfect black body. In this case, the value $\varepsilon = 1$ was used for all the planets and their satellites and the value 0.9 for dwarf planets and all small solar system bodies.

σ is the Stefan-Boltzmann constant $= 5.670373 \times 10^{-8}$ W$m^{-2}K^{-4}$.

η in a first-order approximation corresponds to the thermal inertia and surface roughness, the same value as used in the in the publication of *"TNOs are cool: A survey of the trans-Neptunian region. V. Physical characterization of 18 Plutinos using Herschel-PACS observations"* [69], was used η=1.2.

r is the heliocentric range of the target in AU.

6. Identification Colour Correction Index

   Once the temperatures for all the bodies were known, the colour correction index to use was identified. The indexes for PACS are tabulated in *"PACS Photometer Passbands and Colour Correction Factors for Various Source SEDs"* [97], and are listed in Table 26.

7. Colour Correction

   The last step required to obtain the monochromatic flux densities, is to perform the colour correction by dividing the flux by the colour correction index for the specific wavelength band, see Equation 3, 4 and 5.

$$Flux_{CC}70\mu m = \frac{FluxInBand}{CC_70\mu m} \tag{3}$$

$$Flux_{CC}100\mu m = \frac{FluxInBand}{CC_100\mu m} \tag{4}$$

$$Flux_{CC}160\mu m = \frac{FluxInBand}{CC_160\mu m} \tag{5}$$

Temp. [k]	CC_70 μm	CC_100 μm	CC_160 μm
10000	1.016	1.034	1.074
5000	1.016	1.033	1.074
1000	1.013	1.031	1.072
500	1.011	1.029	1.068
250	1.005	1.023	1.062
100	0.989	1.007	1.042
50	0.982	0.985	1.010
40	0.992	0.980	0.995
30	1.034	0.982	0.976
20	1.224	1.036	0.963
19	1.269	1.051	0.964
18	1.325	1.069	0.967
17	1.396	1.093	0.972
16	1.488	1.123	0.979
15	1.607	1.162	0.990
14	1.768	1.213	1.005
13	1.992	1.282	1.028
12	2.317	1.377	1.061
11	2.816	1.512	1.110
10	3.645	1.711	1.184
9	5.175	2.024	1.300
8	8.497	2.554	1.491
7	17.815	3.552	1.833
6	58.391	5.774	2.528
5	456.837	12.259	4.278

Table 26: Colour correction indexes.

8. Annular Sky Aperture Photometry for Flux STD

For the computation of the flux, photometric errors, better called uncertainties, should be considered. These uncertainties are a result of noise. For a CCD measurement, different types of noise can be presented, e.g. photon noise, readout noise, dark current noise and processing noise [89], but from all these noises the one that dominates over the others is the photon noise of the sky which can be estimated with the Root-Mean-Squared based S/N.

The photometric error is also known as the standard deviation of the aperture photometry, or the background Root-Mean-Squared based S/N [43]. The method used for its calculation consisted of placing several apertures on the sky background around the source and performing aperture photometry, but without subtracting the sky background contribution. A first mean and standard deviation were calculated for these apertures. The apertures with a flux higher than two times the standard deviation were excluded, and the flux was once again calculated with the remaining apertures (without subtracting the sky background contribution). A new mean and a new standard deviation were computed in this iterative process. This new calculated standard deviation is the photometric error or the background RMS based S/N.

The apertures around the source were placed in a 9x9 grid, with an interval of 5

pixels, centred on the fitted coordinates of the source. The "Annular Sky Aperture Photometry" task was used in HIPE, with the same aperture size as the one used for calculating the flux in band.

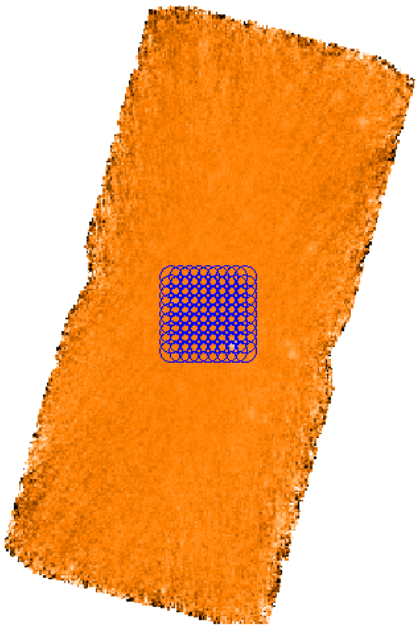

Figure 13: Flux STD calculation - grid.
Observation: 2001 QX322 - ObsID: 1342211621 - HPPUNIMAPB.

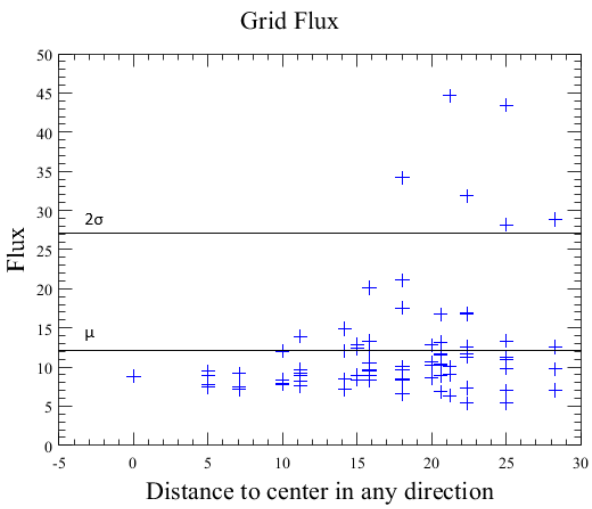

Figure 14: Flux STD calculation - plot fluxes.
Observation: 2001 QX322 - ObsID: 1342211621 - HPPUNIMAPB.

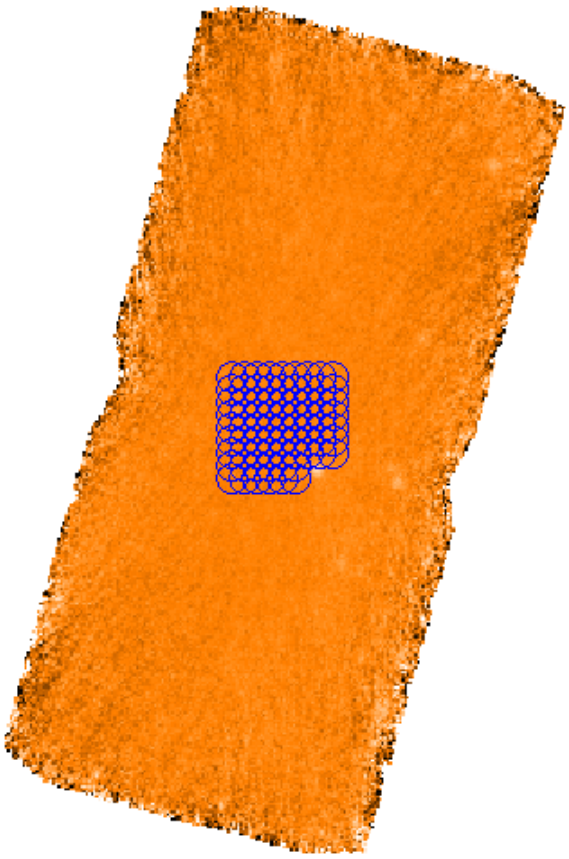

Figure 15: Flux STD calculation - grid after exclusion of apertures by sigma clipping. Observation: 2001 QX322 - ObsID: 1342211621 - HPPUNIMAPB.

Figure 13 shows the aperture radii placed in the 9x9 grid, centred on the source, used for the first photometric calculation.

Figure 14 displays the fluxes in mJy obtained in the first calculation of the aperture photometry, with the mean value line and the $2\times\sigma$ line threshold plotted. We can see that 6 of the calculated fluxes in the grid are over this threshold.

Figure 15 shows the results obtained when the apertures that had fluxes over the threshold had been removed and a new photometric computation performed. The resulting standard deviation of these fluxes as adopted as the standard deviation of the monochromatic flux.

4.1.2 Validation of the Pipeline

In order to assess the calculated flux and to validate the pipeline, a comparison was made between the calculated fluxes and the fluxes from publications, see Appendix B. There were 956 published fluxes from the 1277 observation.

The differences between the calculated and the published fluxes were calculated and the errors displayed accumulatively in Figure 16.

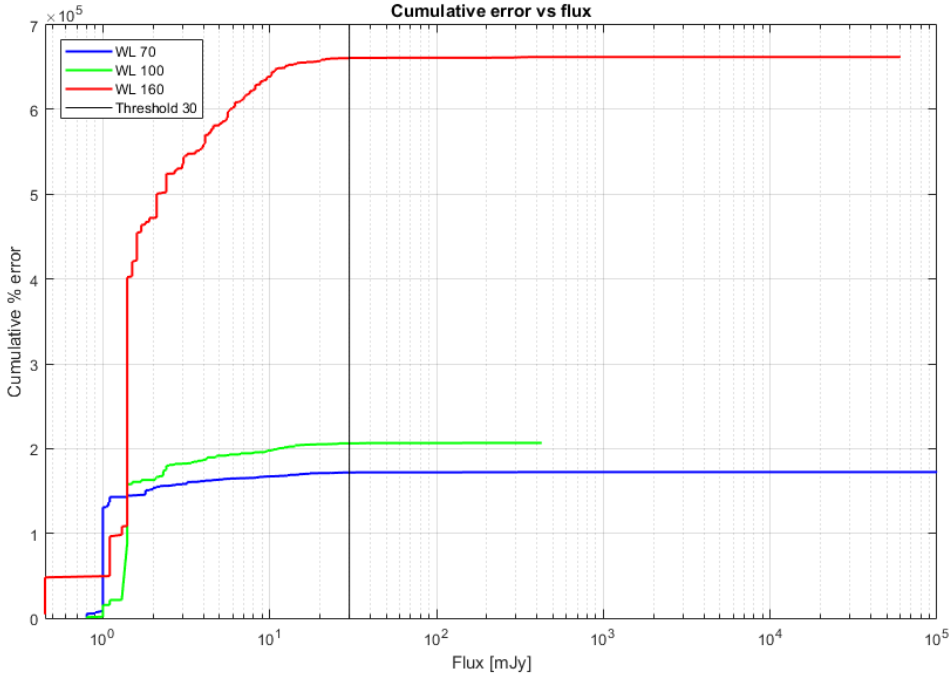

Figure 16: Fluxes vs cumulative errors resulting from the differences between calculated and published fluxes.

From Figure 16, we can see that, unsurprisingly, the largest errors are for those fluxes <10 mJy. The source fitting technique is more accurate when the input coordinates are precise and the sky background noise and contamination are reduced. This is not usually the case for faint sources and this is the reason for the resulting large errors. The fact that the source fitting task does not find the correct centre of a faint target was confirmed when big differences between the calculated and the fitted coordinates for bodies with published observations <10 mJy were detected.

There are different techniques for data reduction and for improving the maps, (e.g. differential and double-differential images) these methods can be found in the publication *"Optimized Herschel/PACS photometer observing and data reduction strategies for moving solar system targets"* [53]. One of the methods proposed "supersky-subtracted image" was tested, but failed since the coordinates were not as precise as were required for the technique of co-adding maps. A future specific pipeline for data reduction and observation of faint bodies should be used.

In Figure 16, we can see that the errors decreased considerably when the fluxes were >20 mJy and there were practically no errors with fluxes >30 mJy. The reason is that the targets are brighter and the source fitting task can obtain precise coordinates for them without confusing them with the background.

To complete the validation of the photometric calculation pipeline, we checked the reliability of the flux density measurements presented here by performing another comparison between fluxes. In this case the fluxes calculated in this work and the published ones were compared with the fluxes from the Herschel Highly Processed Data Product: *"The Herschel/PACS Point Source Catalogue"* (HPPSC) [43].

The Figures 17, 18 and 19 are composed of four plots.

The upper graphics are a direct comparison between the HPPSC flux in the horizontal axis and, on the left side, the calculated flux from this work in the vertical axis and, on the right side, the published flux in the vertical axis. A regression analysis was performed in order to find a function (a straight line) that describes the behaviour of the correlation between the values of these fluxes, this line is represented by black dashed lines. The functional model used can be seen in Equation 6, with a and b constants:

$$y_i = ax_i + b \tag{6}$$

We used the least-squares method to fit the regression line.

In the lower graphics, the percentage differences between the two sets of fluxes (calculated - HPPSC) on the left side and (published - HPPSC) on the right side are presented. A threshold of ±15% was selected in order to account for possible differences between the photometric calculation methods. As we can see, all the differences between the published and the HPPSC fluxes fall inside these limits, supporting the decision to use this threshold.

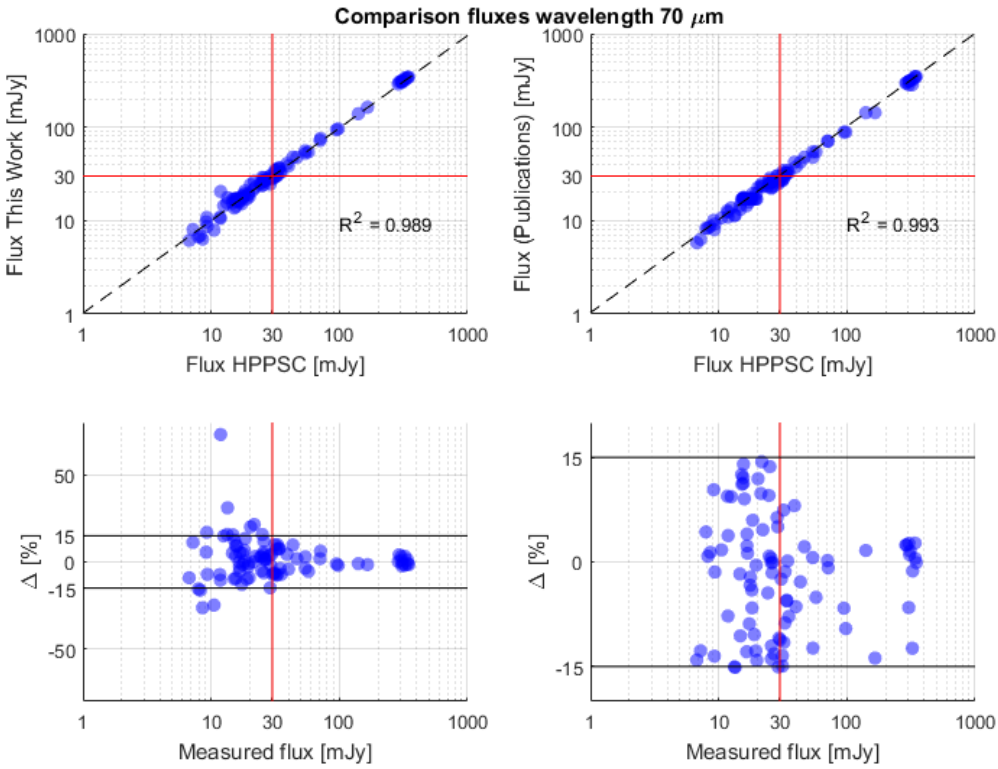

Figure 17: Top graphics: comparison between the 70 μm flux density estimates from the HPPSC and this work (left) and from the HPPSC and those presented in the literature (right), the black dashed lines represent the fitted regression line for each dataset. Bottom graphics: difference in percentage for each data set. The black horizontal lines indicate the thresholds of ±15% between the two fluxes.

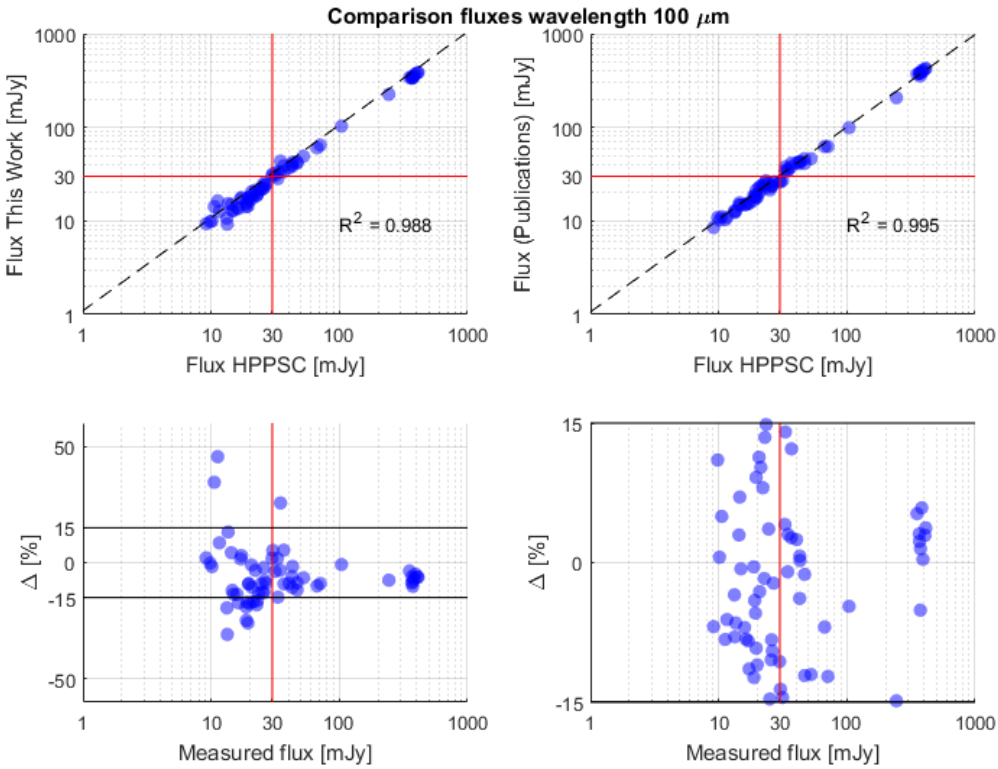

Figure 18: Top graphics: comparison between the 100 μm flux density estimates from the HPPSC and this work (left) and from the HPPSC and those presented in the literature (right), the black dashed lines represent the fitted regression line for each dataset. Bottom graphics: difference in percentage for each data set. The black horizontal lines indicate the thresholds of $\pm 15\%$ between the two fluxes.

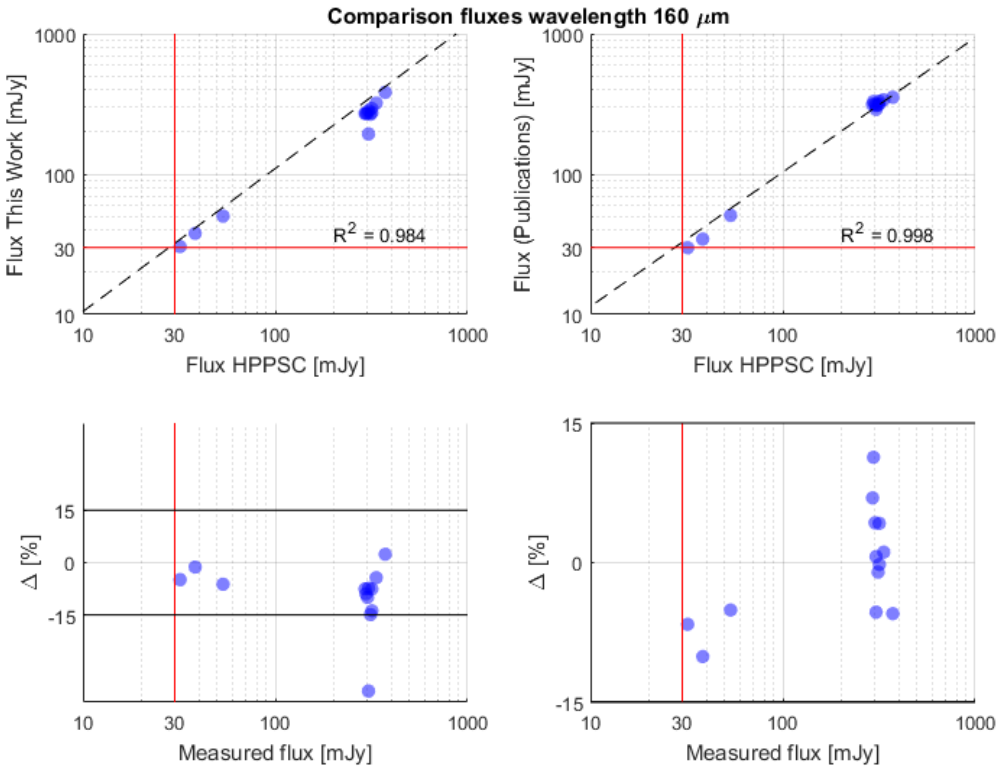

Figure 19: Top graphics: comparison between the 160 μm flux density estimates from the HPPSC and this work (left) and from the HPPSC and those presented in the literature (right), the black dashed lines represent the fitted regression line for each dataset. Bottom graphics: difference in percentage for each data set. The black horizontal lines indicate the thresholds of $\pm 15\%$.

In Figure 17 we see that, for both cases, the value of R-squared is close to one, which indicates that the two sets of fluxes are strongly correlated. We can also see that the errors are higher when the flux value decreases. The differences between the calculated and the HPPSC fluxes over the 25-30 mJy are very small, as it was also concluded when observing Figure 16.

In Figure 18, similar conclusions are reached. R-squared is almost one for both cases and the dispersion of the observations is, as expected, larger at lower fluxes. The differences between the calculated and the HPPSC fluxes over the 25-30 mJy are small except for just one, discrepant observation.

In Figure 19, we see that R-squared is also close to one, even though we have fewer observations than on the two previous graphics, see Figures 17 and 18. We also observe that the differences between the calculated and the HPPSC fluxes for sources brighter than 30 mJy are very small, with the exception of just one discrepant observation. The observation is one of Pluto, with ObsID: 1342191991: it presents a very high photometric standard deviation, see Image 20, consistent with the fact that Pluto crossed the Galactic Plane as seen from Herschel, only 12 degrees from the Galactic Centre, on December 27th 2009 and again on August 12th and October 7th 2010 and was thus in a region of very bright and highly structured background, making calculation of accurate photometry extremely problematic.

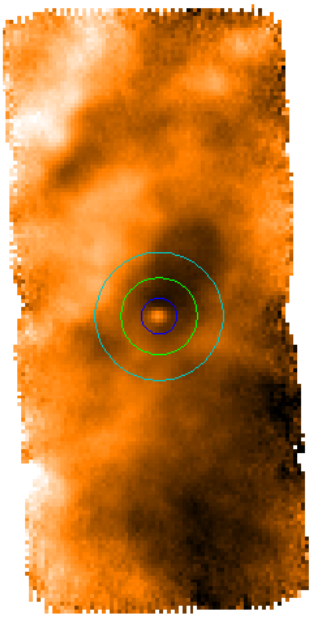

Figure 20: Contaminated sky in the observation of Pluto at a wavelength of 160 μm. Observation: Pluto - ObsID: 1342191991 - HPPUNIMAPR.

We conclude from the validation of the photometric calculation, that a new pipeline for flux consolidation should be created taking into account only the fluxes higher than 25-30 mJy, depending on the degree of structure in the source background.

4.1.3 Flux Consolidation Pipeline

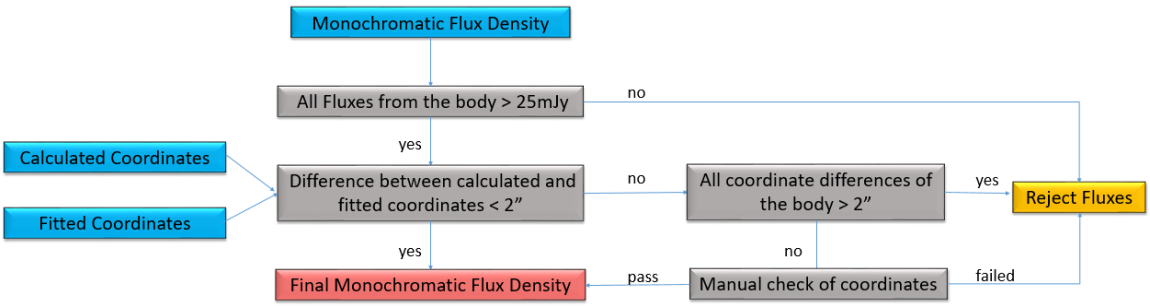

Figure 21: Flux consolidation pipeline.

For the consolidation of the non-faint fluxes, a pipeline was executed, see Figure 21. The first step was to verify that all the fluxes of a target were >25 mJy, in the case that not all the fluxes of the target were over >25 mJy, the target was rejected.

The second step consisted of checking whether or not all the observations of a body had a difference between calculated and fitted coordinates <2”, which was the Herschel Absolute Pointing Error in the early mission phases, although this value improved progressively to $\approx$ 0.8” through the mission [92]. If all the observations of the body had a larger difference this, the target was rejected. When some, but not all of the observations were over this threshold, a manual check was performed to ensure that there was no problem with the

coordinates and that the aperture photometry radii were centred in the target. If this check was passed, the final monochromatic flux densities were obtained.

At the end of the pipeline, the following targets and observations remained, see Table 27.

Wavelength	70 μm	100 μm	160 μm
Total №Obs	139	82	144
Total №Target	31	20	21
Total №new Obs	44	25	56
Total №new Targets	14	10	12

Table 27: Total number of targets and observations after pipeline for flux validation.

In Tables 28, 29 and 30 the targets with new flux values can be found. Most of the new measurements correspond to comets, therefore a particular study of comets was carried out and can be found in the Herschel Catalogue of Solar System Object Observations Explanatory Supplement Volume I.

NAIF ID	Target
1003031	Garradd (C/2009 P1)
1000041	103P/Hartley 2
1002430	Christensen (C/2006 W3)
1000045	45P/Honda-Mrkos-Pajdusakova
1000094	10P/Tempel 2
1003133	PANSTARRS (C/2011 L4)-1
1000079	29P/Schwassmann-Wachmann 1
1000093	9P/Tempel 1
2134340	Pluto
2143707	143707 (2003 UY117)
2000433	433 Eros
2000253	253 Mathilde
2175706	175706 (1996 FG3)
2002060	2060 Chiron

Table 28: List of targets with new fluxes observed at 70 μm.

NAIF ID	Target
1003031	Garradd (C/2009 P1)
1000041	103P/Hartley 2
1000093	9P/Tempel 1
2134340	Pluto
899	Neptune
2120347	120347 (2004 SB60)-1
2050000	50000 Quaoar
2000433	433 Eros
2000253	253 Mathilde
2175706	175706 (1996 FG3)

Table 29: List of targets with new fluxes observed at 100 μm.

NAIF ID	Target
1003031	Garradd (C/2009 P1)
1000041	103P/Hartley 2
1000093	9P/Tempel 1
899	Neptune
2000433	433 Eros
2000253	253 Mathilde
2175706	175706 (1996 FG3)
1002430	Christensen (C/2006 W3)
1000045	Honda-Mrkos-Pajdusakova-1
1000094	10P/Tempel 2
1003133	PANSTARRS (C/2011 L4)-1
1000079	29P/Schwassmann-Wachmann 1

Table 30: List of targets with new fluxes observed at 160 μm.

4.1.4 Validation of the Consolidation of Fluxes

In this subsection, we perform a validation of the flux consolidation pipeline, comparing its output with that of available publications, see Appendix B.

In Figures 22, 23 and 24, the comparison between the validated calculated fluxes and the publications are presented, with figures considering the same characteristics as the ones shown in section 4.1.2 Validation of the Pipeline.

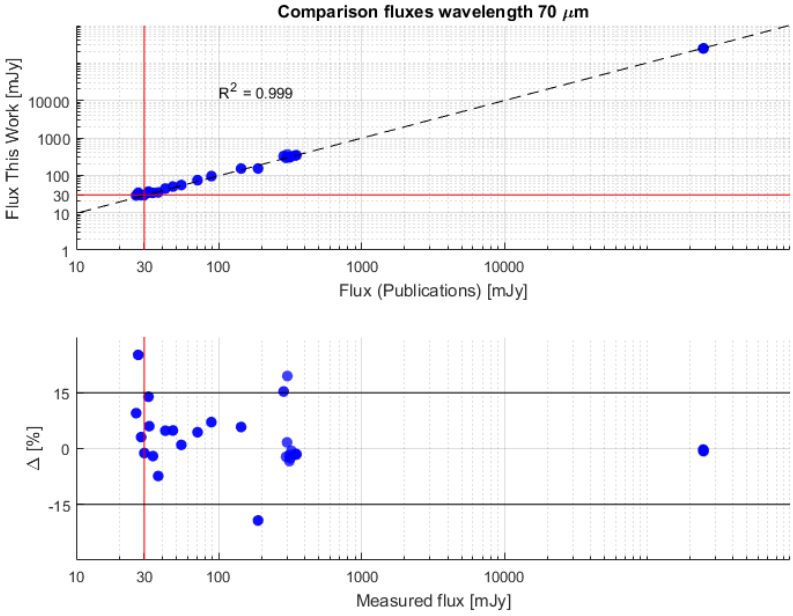

Figure 22: Top graphic: comparison between the 70 μm flux density estimates from this work and those presented in the literature, the black dashed lines represent the fitted regression line for the dataset. Bottom graphic: difference in percentage for the data set. The black horizontal lines indicate the thresholds $\pm 15\%$ agreement.

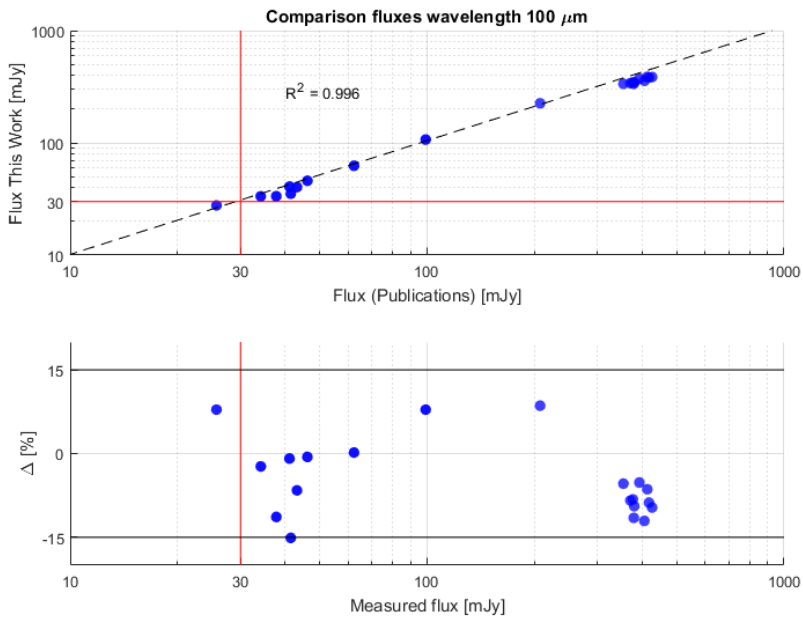

Figure 23: Top graphic: comparison between the 100 μm flux density estimates from this work and those presented in the literature, the black dashed lines represent the fitted regression line for the dataset. Bottom graphic: difference in percentage for the data set. The black horizontal lines indicate the thresholds $\pm 15\%$ agreement.

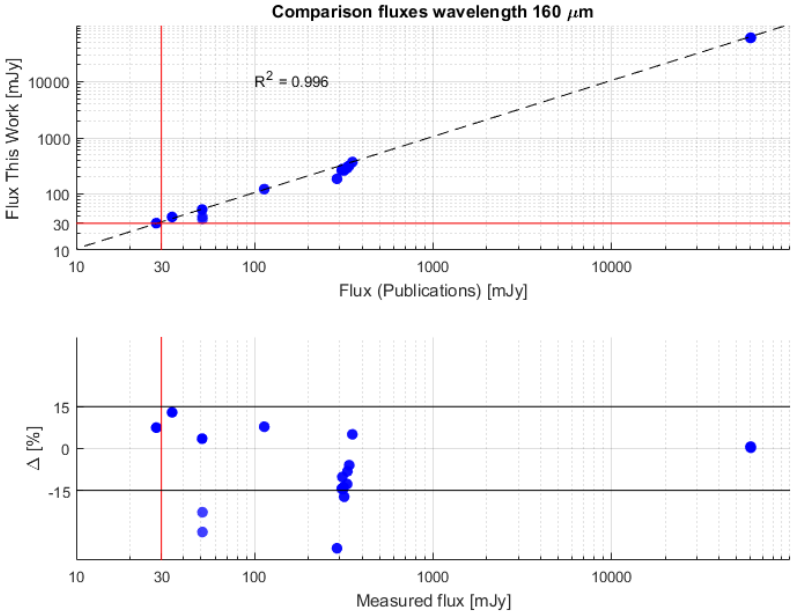

Figure 24: Top graphic: comparison between the 160 μm flux density estimates from this work and those presented in the literature, the black dashed lines represent the fitted regression line for the dataset. Bottom graphic: difference in percentage for the data set. The black horizontal lines indicate the thresholds $\pm 15\%$.

In Figures 22, 23 and 24, we can see two graphics for each figure. The upper one is a direct comparison between the flux obtained from publications, in the horizontal axis and the validated calculated flux from this work, in the vertical axis, the black dashed lines represent the fitted regression line for the dataset. In the lower graphic, the percentage difference between the two fluxes (calculated - published) is presented. The threshold of ± 15 is used to indicate reasonable agreement between the results obtained with different methods.

In Figure 22, we can see that, in the first graphic, the R-squared is almost equal to one, hence the two sets of fluxes are strongly correlated. In the second graphic we can observe the percentage of the differences between the fluxes, most of the values are between the two thresholds which confirms the similarities between these two sets of fluxes, but three values are over the ± 15 threshold and must be analysed further.

The three values correspond to the fluxes from Phoebe observation ID: 134221248 and 47171(1999 TC36) observation IDs: 1342199491 and 1342199630.

Three different methods were used, in addition to the one described in the photometric calculation pipeline, to verify that there were no errors in the calculation of the fluxes. The three methods were the following:

1. Change of map product from Unimap to JScanam to verify that the cause of the error is not in the map product.
2. Perform the photometry manually, identifying manually the centre of the body to discard the possibility that there is an error in the coordinates.
3. Perform the photometry with an aperture radius = FWHM instead of radius =

FWHM×4, to ensure that is not a problem with the selection of the radii and contamination from the sky background.

The fluxes of these three observations were re-estimated following the three different methods mentioned above. The resulting fluxes had similar values as the ones calculated through the photometric calculation pipeline and therefore it can be assumed that the computation of the fluxes were correct.

In Figure 23 we can see that both of the sets of fluxes are strongly correlated, since the R-squared is close to one and there are no differences bigger than the thresholds.

In Figure 24 we see, once again, the two sets of fluxes are strongly correlated since the R-squared is close to one and only three observations are over the threshold of ±15% difference. These observations correspond to Pluto, with the following ObsIDs: 1342191991, 1342241418 and 1342241420.

For ObsID 1342191991, there was a very high photometric standard deviation, indicating that the sky background was very contaminated, see Image 20.

For the other two observations (1342241418 and 1342241420), the three different verification methods were performed and similar calculated fluxes were obtained, which indicates that the calculation of the flux had no errors.

As a conclusion, we have proved that the consolidated fluxes show good correspondence with the published ones, the computed fluxes are within ±15% difference with respect to the published ones. All of the outlier fluxes have been verified as being correctly measured, therefore this pipeline gives satisfactory fluxes >30 mJy and can be applied to other bodies of the Solar System.

4.2 Images Included in the Catalogue

For each of the new flux values, see Tables 27, 28, 29 and 30, there will be three images included in the catalogue, excluding the case of the new fluxes of comets, as more detailed analysis was performed in the Herschel Catalogue of Solar System Object Observations Explanatory Supplement Volume I. The three images will have the following structure:

1. **ObsID -ProductID.png:** Corresponding to the image of the body at a specific observing wavelength.
2. **ObsID -ProductID-ApPhot.png:** Corresponding to the image of the body at a specific observing wavelength, with the representation of the aperture radius, inner and outer radius of the sky annulus, described from smaller to larger, used to calculate the flux of the body by using the aperture photometry method, see Figure 12.
3. **ObsID -ProductID-Stdv-F.png** Corresponding to the image of the body at a specific observing wavelength with the representation of the aperture radius grid after exclusion of apertures for calculating the Flux STD, see Figure 15.

ObsID was defined in section 3.2.2. Ancillary Information. ProductID corresponds to Level-2 data products Blue/Red (HPPPMB/HPPPMR) depending on the observing wavelength (blue for 70 and 100 μm and red for 160 μm) or Level-2.5 data products Blue/Red (HPPUNIMAPB/HPPUNIMAPR) depending on the observing wavelength (blue for 70 and 100 μm and red for 160 μm).

5 Results

The aim of the catalogue is to facilitate the study and interpretation of the object observations performed by Herschel. In this Explanatory Supplement a general analysis the catalogue data will be performed.

5.1 General Analysis of the Catalogue Data

In this subsection some of data from the catalogue will be analysed.

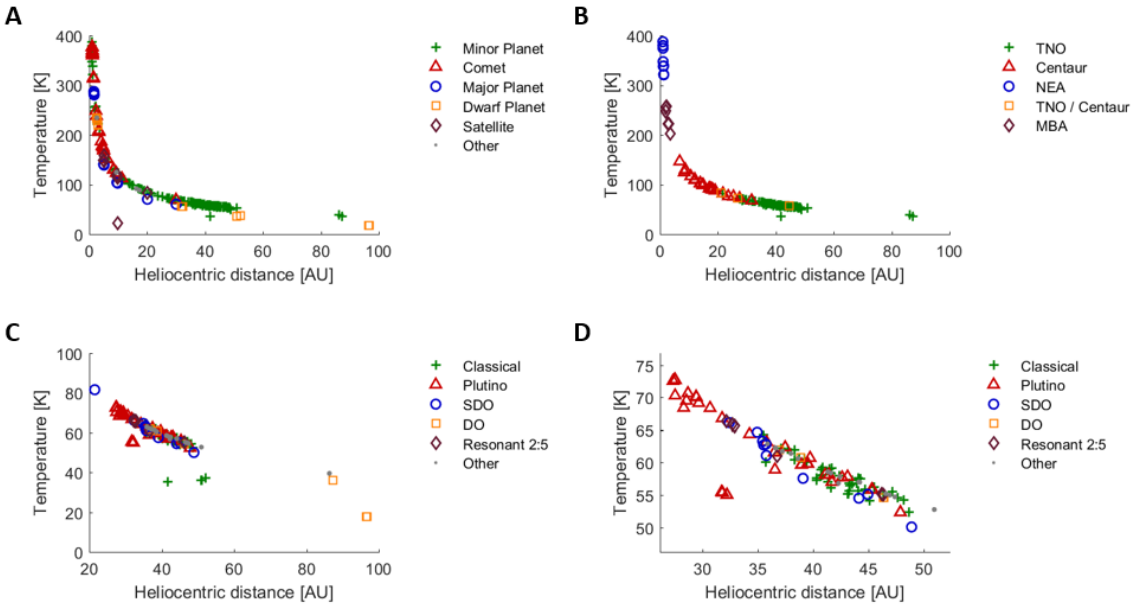

Figure 25: Comparison of the SSOO - calculated temperature vs heliocentric distance. (A) All observations, major class type. (B) Minor planets, dynamical class. (C) TNOs, second dynamical class. (D) TNOs between 23 and 52 AU, main cluster in (C). We see the expected correlation, although there are some outliers.

	A	B	C / D
ρ	-0.95	-0.98	-0.81
significance	p <0.001	p<0.001	p<0.001
N^oObservations	1692	1102	953
N^oTargets	170	137	105

Table 31: Comparison of the SSOO - temperature vs heliocentric distance - statistics.

In Figure 25, the temperature is compared to the heliocentric distance using the Spearman's rank correlation coefficient which measures the correlation between two variables. The statistical results and the number of observations and targets can be seen in table 31.

Graphic A shows the relationship between heliocentric distance and temperature across all the observations in the catalogue, separated by major classes. As expected, the temperature decreases with the increasing heliocentric distance in an almost monotonic relationship with

a very strong anti-correlation of ρ = -0.95, see Table 31, with Enceladus being the only extreme outlier. In the graphic B, the rank correlation is even stronger than A, ρ = -0.98, graphic B also shows a clear distinction between the dynamical classes of the minor planets. In graphics C and D, the anti-correlation is weaker than A and B, but still a "very strong" monotonic correlation and the same relation is maintained: as expected, the temperature decreases with increasing heliocentric distance.

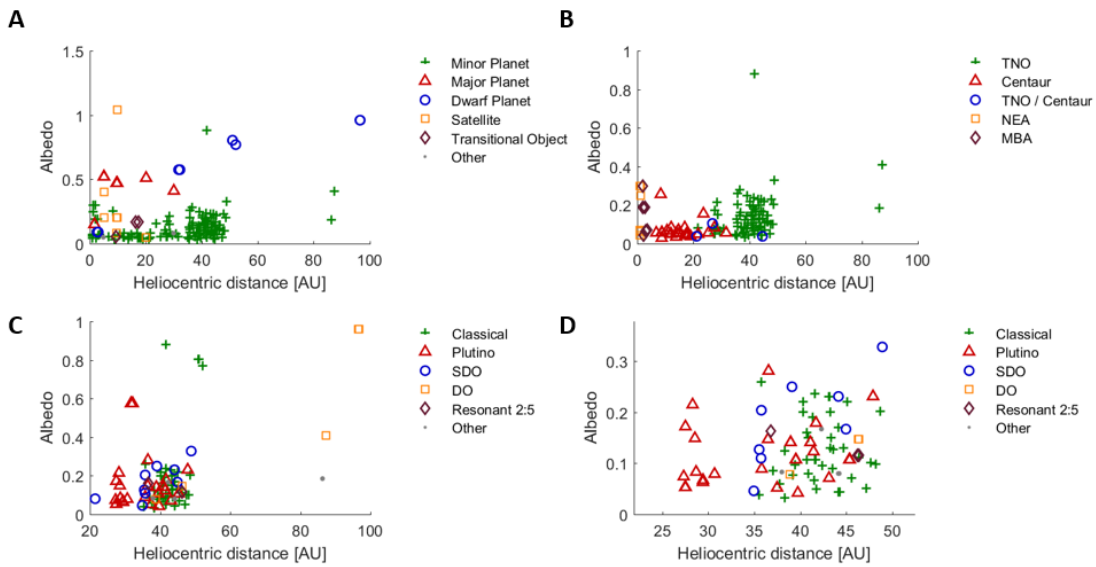

Figure 26: Comparison of the SSOO - albedo vs heliocentric distance. (A) All observations, major class type. (B) Minor planets, dynamical class. (C) TNOs, second dynamical class. (D) TNOs between 23 and 52 AU, main cluster in (C).

	A	B	C / D
ρ	0.11	0.40	0.22
significance	p<0.001	p<0.001	p<0.001
N^oObservations	1303	903	756
N^oTargets	132	112	81

Table 32: Comparison of the SSOO - albedo vs heliocentric distance - statistics.

A comparison between the albedo and the distance was performed in Figure 26, using the Spearman rank correlation. The statistical results and the number of observations and targets can be seen in the table 32.

There is a very weak, positive monotonic correlation between albedo and heliocentric distance across all the graphics. Although in graphic A we see the dwarf planets albedo increases with the distance, having a ρ = 0.93 and p < 0.001 for the 120 observations of the 5 targets. In graphic D for the SDO (ρ = 0.84 and p < 0.001 for the 72 observations of the 9 targets) and for the DO (ρ = 0.95 and p < 0.001 for the 45 observations of the 4 targets) it is obtained a very strong monotonic correlation between the distance and the albedo. This could maybe be a general characteristic of the non resonant TNOs, although there is also a strong selection effect involved as only the TNOs that are largest and with highest albedo will be discovered at the greatest distances from the Sun, although these will

also be the TNOs with the lowest fluxes in the Herschel bands, as a higher albedo implies a lower emissivity and thus less thermal emission.

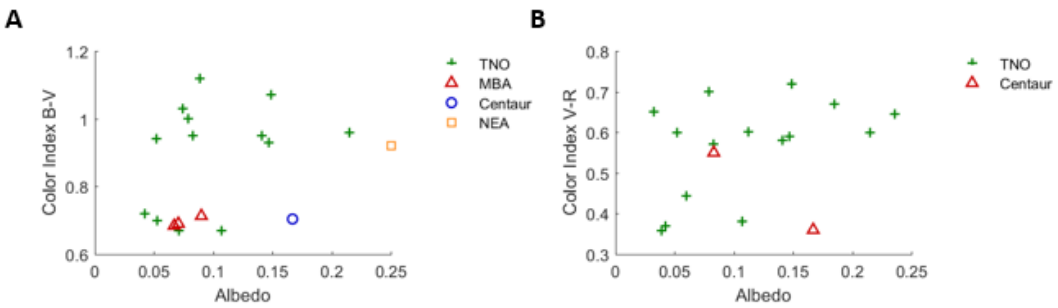

Figure 27: Comparison of the SSOO - colour indexes vs albedo. (A) Minor planets, dynamical class. (B) Minor planets, dynamical class.

	A	B
ρ	0.14	0.26
significance	p< 0.084	p< 0.002
N^oObservations	156	147
N^oTargets	18	17

Table 33: Comparison of the SSOO - colour indexes vs albedo - statistics.

The distribution of colour and albedo is seen in Figure 27, and with the statistics and number of observations and targets presented in Table 33. Graphic A appears to be bimodal, as previously reported by Lacerda et al. (2015) [57]. Most of the TNOs have a larger B-V colour index than the rest of the minor planets. A larger B-V indicates that a body has red colour and cold temperatures. In graphic B the V-R colour index seems higher too for the majority of TNOs: a higher V-R indicates a red and cold body, the same results as for B-V, as shown in graphic A.

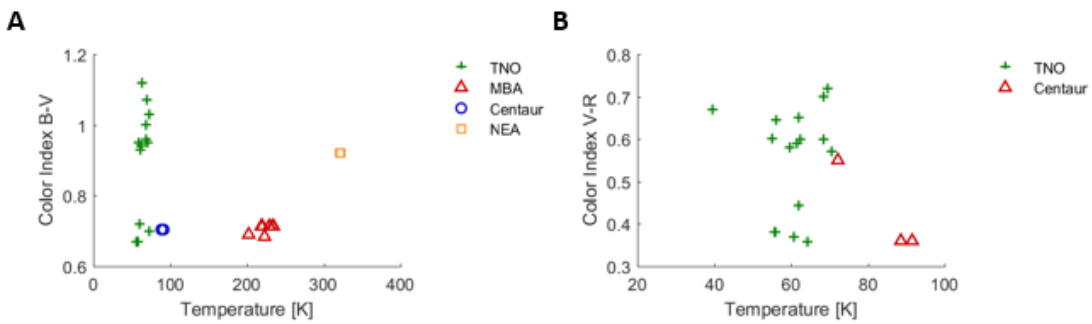

Figure 28: Comparison of the SSOO - colour indexes vs temperature. (A) B-V against temperature for Minor planets, split by dynamical class. (B) V-R for Minor planets, split by dynamical class.

	A	B
ρ	-0.12	-0.27
significance	p< 0.14	p<0.001
N^oObservations	156	147
N^oTargets	18	17

Table 34: Comparison of the SSOO - colour index vs temperature - statistics.

In Figure 28 the relation between colour indexes and temperature is studied. There is a very weak, negative correlation between B-V colour index and temperature (considering TNOs, MBAs, Centaurs and NEA), and a weak one between V-R colour index and temperature (considering only TNOs and Centaurs). Both graphics appear bimodal, more clearly in graphic A than in graphic B. In graphic A we observe, unsurprisingly, that the Main Belt Asteroids have a higher temperature and a lower B-V index than the majority of TNOs, which corresponds to a blue colour and higher temperatures. In contrast, the majority of the TNOs present a larger B-V colour index and a lower temperature.

As a conclusion of this general analysis of the catalogue data, as expected, the observations and targets in the catalogue show a monotonic relationship between distance and temperature. As expected with increasing distance, the temperature decreases. The albedo does not seem to be strongly dependent on the heliocentric distances, except for the dwarf planets and the SDO and DO Trans-Neptunian Objects: this physical quantity could potentially be a defining characteristic of these bodies. The colour indexes show a bimodal behaviour dividing TNOs from the other minor planets and defining them as red cold bodies.

5.2 Conclusions

The aim this work was to use all Herschel's Solar System science observations to create the Herschel Catalogue of Solar System Object Observations. Its goal is to become a reference archive from which information may be extracted for comparative statistical studies, modelling and further exploitation of the data.

The HCSSOO was created by gathering together all of the SSOO observed by Herschel with their classification, ancillary information and relevant physical characteristics but also, the completion of missing photometry was carried out providing a working photometric calculation and flux consolidation pipeline which can be satisfactory applied to other bodies of the Solar System for obtaining fluxes >30 mJy.

Furthermore, this work also verifies that the extraction of data from the HSCSSOO can be used for analytical studies and other research purposes to widen our knowledge of the Solar System.

5.3 Problems Encountered

During the photometric calculation pipeline some significant issues were encountered that are described here, both as caveats on the data and to explain how they were resolved within this work.

5.3.1 Sky Contamination

One common problem when performing aperture photometry is the sky contamination that occurs when light from other sources falls within the aperture radius. For example, in Figure 29 we can see comet 29P/Schwassmann-Wachmann 1. The comet is the brightest source in the field of view, but surrounded by background galaxies that contaminate the photometry.

When the photometric calculation is performed, Figure 30, the galaxies fall inside the aperture radius. Therefore, the resulting flux from this aperture will not only have the flux from the target but also the flux from the galaxies. The way to resolve this is to perform aperture photometry and measure independently the flux from these galaxies, see Figure 31, and subtracting their values from the total flux of the comet.

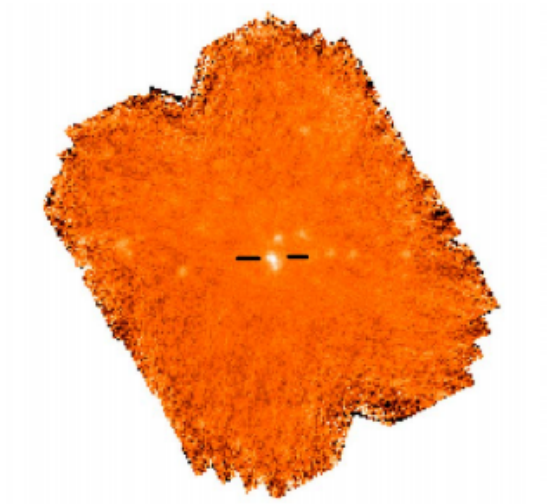

Figure 29: Example of sky contamination - identifying the source.
Observation: 29P/Schwassmann-Wachmann 1 - ObsID: 1342212282 - HPPUNIMAPR.

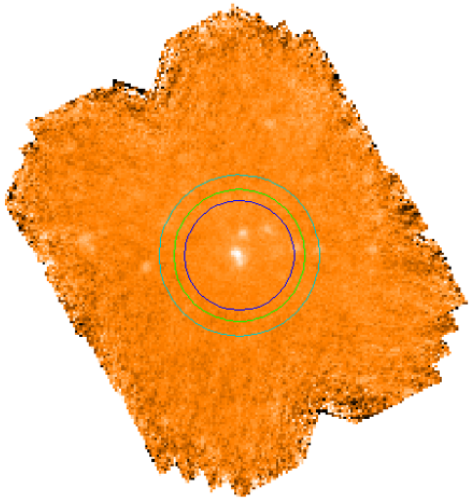

Figure 30: Example of sky contamination - aperture photometry.
Observation: 29P/Schwassmann-Wachmann 1 - ObsID: 1342212282 - HPPUNIMAPR.

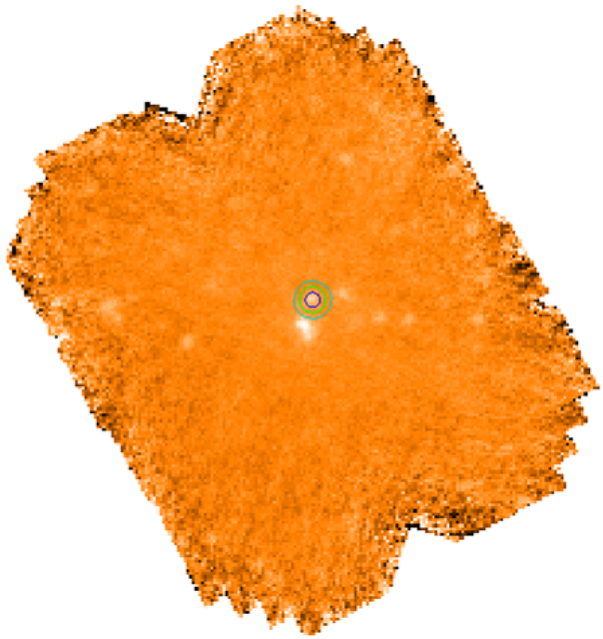

Figure 31: Example of sky contamination - extraction of the contamination. Observation: 29P/Schwassmann-Wachmann 1 - ObsID: 1342212282 - HPPUNIMAPR.

5.3.2 Faint Bodies

Performing photometry on faint bodies was very complicated, which is why at the end only fluxes>30 mJy were validated: because they are so faint these sources can be confused with the background noise.

For all the faint bodies for which we are unable to give flux values, the following two lists indicate the bodies for which fluxes will not be measurable because they are either non-detected, or only marginally detected at best:

The following targets are considered as possible marginal detections:

- 2001 FZ173, Müller et al. (in preparation)
- 2005 RM43, Müller et al. (in preparation)
- 2004 PG115, Müller et al. (in preparation)

The following are targets considered non detections:

- 24835(1995 SM55), Vilenius et al. 2018
- 19308 (1996 TO66), Vilenius et al. 2018
- 1999 CD158, Vilenius et al. 2018
- 2001 QX322, Kiss et al. (in preparation)
- 2002 CY224, Kiss et al. (in preparation)

5.3.3 Eliminated Observations

As it has been seen in section 4.1.1. Photometric Calculation Pipeline, in the first part of Coordinate Calculation, there are some observations were the target does not appear inside the map, or cannot be identified clearly. These observations were marked and eliminated from the photometric calculation. The ObsIDs of the eliminated observations are the following:

- 1342211791
- 1342211792
- 1342224620
- 1342224621
- 1342224622
- 1342224623
- 1342224837
- 1342224838
- 1342224839
- 1342224840
- 1342232729
- 1342232730
- 1342234207
- 1342234208
- 1342234435
- 1342234436
- 1342236891
- 1342236892
- 1342237436

Other observations, see Figures 32 and 33, presented errors and therefore were excluded from the computation of the fluxes.

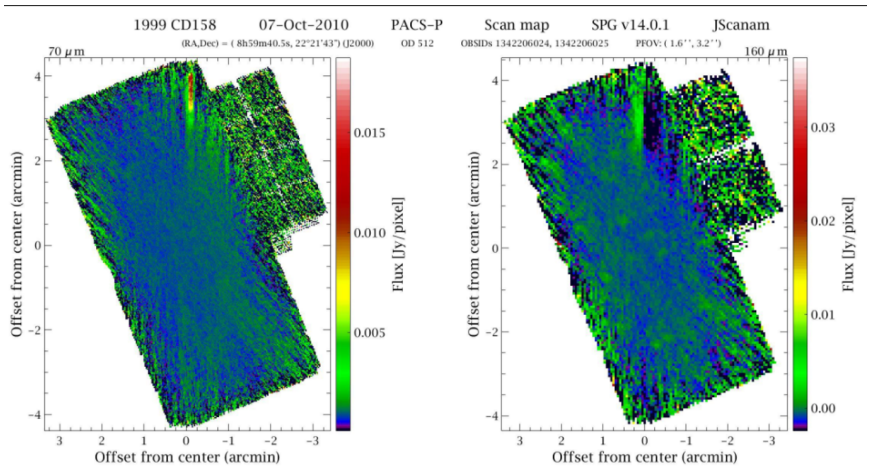

Figure 32: Eliminated observations - 1999 CD158 - ObsIDs: 1342206024 / 1342206025.

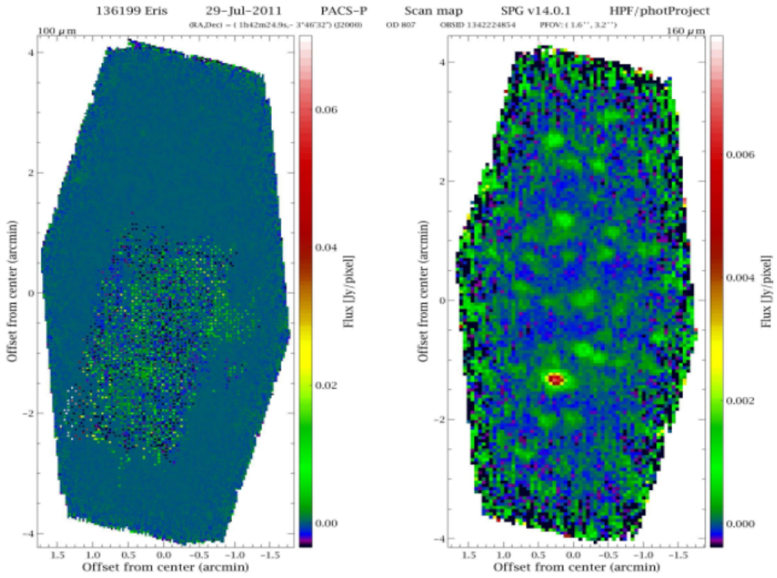

Figure 33: Eliminated observations - 136199 Eris - ObsID: 1342224854.

Another observation that was eliminated was the one shown in Figure 34, which was a very special case, observed in a unique way, because the asteroid made an exceptionally close approach to the Earth and was moving much faster than the maximum permitted tracking speed of the observatory. To observe it the satellite slewed along the track of the asteroid, capturing it as it crossed the field of view.

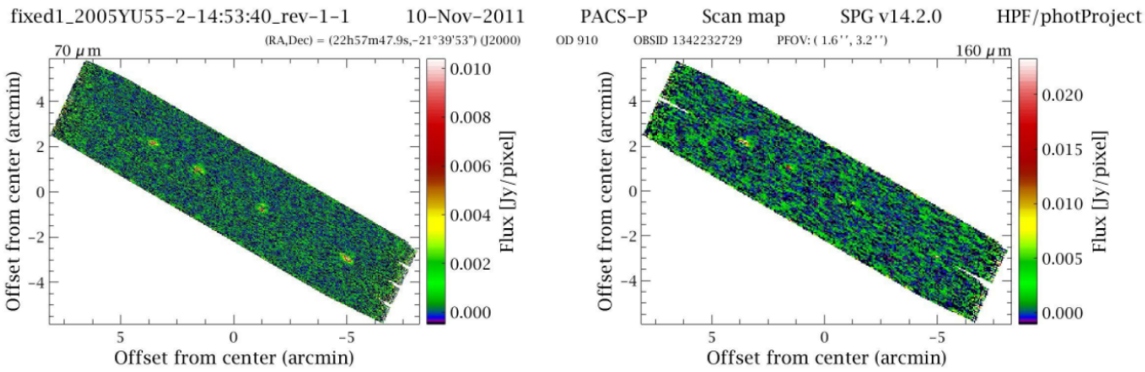

Figure 34: Eliminated observations - 2005 YU55 - ObsIDs: 1342232729 / 1342232730.

References

[1] ESA - Herschel - Data Products Overview. https://www.cosmos.esa.int/web/herschel/data-products-overview.

[2] ESA - Herschel - Documentation HIPE. http://herschel.esac.esa.int/Docs/Herschel/html/ch08s05.html.

[3] ESA - Herschel - HIPE download. https://www.cosmos.esa.int/web/herschel/hipe-download.

[4] ESA - Herschel - Postcard Gallery. http://archives.esac.esa.int/hsa/aio/doc/postcardGallery.html.

[5] ESA - Herschel - Status Report -April 2013. http://sci.esa.int/herschel/51924-herschel-status-report-04-2013/.

[6] ESA - Herschel Documentation AOT. http://herschel.esac.esa.int/Docs/Herschel/html/ch06s04.html#sec1:useAOTs.

[7] ESA - Herschel Fact sheet. http://sci.esa.int/herschel/31361-fact-sheet/.

[8] ESA - Herschel Instruments. http://www.esa.int/Our_Activities/Space_Science/Herschel/Instruments.

[9] ESA - Herschel Mission Overview and Key Programmes. http://herschel.esac.esa.int/Publ/2008/SPIE2008_Herschel_talk.pdf.

[10] ESA - Herschel Mission Overview and Key Programmes. http://herschel.esac.esa.int/Publ/2008/SPIE2008_Herschel_talk.pdf.

[11] ESA - Herschel "Must-Do" Programmes. https://www.cosmos.esa.int/web/herschel/must-do-programmes.

[12] ESA - Herschel Observing Key Programmes. https://www.cosmos.esa.int/web/herschel/key-programmes.

[13] ESA - Herschel Observing Log. http://herschel.esac.esa.int/obslog/.

[14] ESA - Herschel Science Archive. http://archives.esac.esa.int/hsa/whsa/.

[15] HIPE 4.20. Fitting Sources. http://herschel.esac.esa.int/hcss-doc-12.0/.

[16] HIPE 4.21. Aperture Photometry. http://herschel.esac.esa.int/hcss-doc-12.0/.

[17] IAU - Minor Planet Center - MPC Index . https://minorplanetcenter.net/iau/TheIndex.html.

[18] International Astronomical Union - Naming Solar System Objects. https://www.iau.org/public/themes/naming/.

[19] Johnstonsarchive - List of Known Trans-Neptunian Objects. http://www.johnstonsarchive.net/astro/sslist.html.

[20] JPL, California Institute of Technology - Solar System Dynamics - HORIZONS Web-Interface. https://ssd.jpl.nasa.gov/horizons.cgi#top.

[21] NASA - JPL - NAIF Integer ID codes . https://naif.jpl.nasa.gov/pub/naif/toolkit_docs/C/req/naif_ids.html#Planets%20and%20Satellites.

[22] NASA Herschel Science Center's Portal to the Cool Universe - About Herschel. https://www.herschel.caltech.edu/page/about.

[23] NASA Herschel Science Center's Portal to the Cool Universe - Instruments. https://www.herschel.caltech.edu/page/instruments.

[24] TNOs are cool public database. http://public-tnosarecool.lesia.obspm.fr/Published-results.html.

[25] Unimap Home Page. http://infocom.uniroma1.it/unimap/.

[26] M. A. Barucci, F. Merlin, D. Perna, A. Alvarez-Candal, T. Müller, M. Mommert, C. Kiss, S. Fornasier, P. Santos-Sanz, and E. Dotto. The extra red plutino (55638) 2002 VE_{95}. *AAp*, 539:A152, March 2012.

[27] N. Biver, J. Crovisier, D. Bockelée-Morvan, S. Szutowicz, D. C. Lis, P. Hartogh, M. de Val-Borro, R. Moreno, J. Boissier, M. Kidger, M. Küppers, G. Paubert, N. Dello Russo, R. Varvreck, and H. Weaver. Ammonia and other parent molecules in comet 10P/Tempel 2 from Herschel/HIFI and ground-based radio observations. *AAp*, 539:A68, March 2012.

[28] D. Bockelée-Morvan, N. Biver, J. Crovisier, D. C. Lis, P. Hartogh, R. Moreno, M. de Val-Borro, G. A. Blake, S. Szutowicz, J. Boissier, J. Cernicharo, S. B. Charnley, M. Combi, M. A. Cordiner, T. de Graauw, P. Encrenaz, C. Jarchow, M. Kidger, M. Küppers, S. N. Milam, H. S. P. Müller, T. G. Phillips, and M. Rengel. Searches for HCl and HF in comets 103P/Hartley 2 and C/2009 P1 (Garradd) with the Herschel Space Observatory. *AAp*, 562:A5, February 2014.

[29] D. Bockelée-Morvan, N. Biver, J. Crovisier, D. C. Lis, P. Hartogh, R. Moreno, M. de Val-Borro, G. A. Blake, S. Szutowicz, J. Boissier, J. Cernicharo, S. B. Charnley, M. Combi, M. A. Cordiner, T. de Graauw, P. Encrenaz, C. Jarchow, M. Kidger, M. Küppers, S. N. Milam, H. S. P. Müller, T. G. Phillips, and M. Rengel. Searches for HCl and HF in comets 103P/Hartley 2 and C/2009 P1 (Garradd) with the Herschel Space Observatory. *AAp*, 562:A5, February 2014.

[30] D. Bockelée-Morvan, N. Biver, B. Swinyard, M. de Val-Borro, J. Crovisier, P. Hartogh, D. C. Lis, R. Moreno, S. Szutowicz, E. Lellouch, M. Emprechtinger, G. A. Blake, R. Courtin, C. Jarchow, M. Kidger, M. Küppers, M. Rengel, G. R. Davis, T. Fulton, D. Naylor, S. Sidher, and H. Walker. Herschel measurements of the D/H and $^{16}O/^{18}O$ ratios in water in the Oort-cloud comet C/2009 P1 (Garradd). *AAp*, 544:L15, August 2012.

[31] D. Bockelée-Morvan, P. Hartogh, J. Crovisier, B. Vandenbussche, B. M. Swinyard, N. Biver, D. C. Lis, C. Jarchow, R. Moreno, D. Hutsemékers, E. Jehin, M. Küppers, L. M. Lara, E. Lellouch, J. Manfroid, M. de Val-Borro, S. Szutowicz, M. Banaszkiewicz, F. Bensch, M. I. Blecka, M. Emprechtinger, T. Encrenaz, T. Fulton, M. Kidger, M. Rengel, C. Waelkens, E. Bergin, G. A. Blake, J. A. D. L. Blommaert, J. Cernicharo, L. Decin, P. Encrenaz, T. de Graauw, S. Leeks, A. S. Medvedev, D. Naylor, R. Schieder, and N. Thomas. A study of the distant activity of comet C/2006 W3 (Christensen) with Herschel and ground-based radio telescopes. *AAp*, 518:L149, July 2010.

[32] T. Cavalíe, H. Feuchtgruber, E. Lellouch, M. de Val-Borro, C. Jarchow, R. Moreno, P. Hartogh, G. Orton, T. K. Greathouse, F. Billebaud, M. Dobrijevic, L. M. Lara, A. González, and H. Sagawa. Spatial distribution of water in the stratosphere of Jupiter from Herschel HIFI and PACS observations. *AAp*, 553:A21, May 2013.

[33] T. Cavalíe, R. Moreno, E. Lellouch, P. Hartogh, O. Venot, G. S. Orton, C. Jarchow, T. Encrenaz, F. Selsis, F. Hersant, and L. N. Fletcher. The first submillimetre observation of CO in the stratosphere of Uranus. *AAp*, 562:A33, February 2014.

[34] R. Courtin, B. M. Swinyard, R. Moreno, T. Fulton, E. Lellouch, M. Rengel, and P. Hartogh. First results of Herschel-SPIRE observations of Titan. *AAp*, 536:L2, December 2011.

[35] M. de Val-Borro, D. Bockelée-Morvan, E. Jehin, P. Hartogh, C. Opitom, S. Szutowicz, N. Biver, J. Crovisier, D. C. Lis, L. Rezac, T. de Graauw, D. Hutsemékers, C. Jarchow, M. Kidger, M. Küppers, L. M. Lara, J. Manfroid, M. Rengel, B. M. Swinyard, D. Teyssier, B. Vandenbussche, and C. Waelkens. Herschel observations of gas and dust in comet C/2006 W3 (Christensen) at 5 AU from the Sun. *AAp*, 564:A124, April 2014.

[36] M. de Val-Borro, L. Rezac, P. Hartogh, N. Biver, D. Bockelée-Morvan, J. Crovisier, M. Küppers, D. C. Lis, S. Szutowicz, G. A. Blake, M. Emprechtinger, C. Jarchow, E. Jehin, M. Kidger, L.-M. Lara, E. Lellouch, R. Moreno, and M. Rengel. An upper limit for the water outgassing rate of the main-belt comet 176P/LINEAR observed with Herschel/HIFI. *AAp*, 546:L4, October 2012.

[37] R. Duffard, N. Pinilla-Alonso, P. Santos-Sanz, E. Vilenius, J. L. Ortiz, T. Müller, S. Fornasier, E. Lellouch, M. Mommert, A. Pal, C. Kiss, M. Mueller, J. Stansberry, A. Delsanti, N. Peixinho, and D. Trilling. "TNOs are Cool": A survey of the trans-Neptunian region. XI. A Herschel-PACS view of 16 Centaurs. *AAp*, 564:A92, April 2014.

[38] Katrina Exter. Quick-Start Guide To Herschel-PACS the Photometer. *Herschel Space Observatory*, 2017.

[39] H. Feuchtgruber, E. Lellouch, G. Orton, T. de Graauw, B. Vandenbussche, B. Swinyard, R. Moreno, C. Jarchow, F. Billebaud, T. Cavalié, S. Sidher, and P. Hartogh. The D/H ratio in the atmospheres of Uranus and Neptune from Herschel-PACS observations. *AAp*, 551:A126, March 2013.

[40] S. Fornasier, D. Lazzaro, A. Alvarez-Candal, C. Snodgrass, G. P. Tozzi, J. M. Carvano, Y. Jiménez-Teja, J. S. Silva, and D. M. Bramich. The Centaur 10199 Chariklo: investigation into rotational period, absolute magnitude, and cometary activity. *AAp*, 568:L11, August 2014.

[41] S. Fornasier, E. Lellouch, T. Müller, P. Santos-Sanz, P. Panuzzo, C. Kiss, T. Lim, M. Mommert, D. Bockelée-Morvan, E. Vilenius, J. Stansberry, G. P. Tozzi, S. Mottola, A. Delsanti, J. Crovisier, R. Duffard, F. Henry, P. Lacerda, A. Barucci, and A. Gicquel. TNOs are Cool: A survey of the trans-Neptunian region. VIII. Combined Herschel PACS and SPIRE observations of nine bright targets at 70-500 μm. *AAp*, 555:A15, July 2013.

[42] Marton; G., Calzoletti; L., Pérez García; A. M., Kiss; C., Paladini; R., Altieri; B., Sanchez Portal; M., and Kidger; the Herschel Point Source Catalogue Work-

ing Group. The Herschel/PACS Point Source Catalogue Explanatory Supplement. *ArXiv e-prints*, May 2017.

[43] G. Marton, L. Calzoletti, A. M. Perez Garcia, R. Paladini C. Kiss, B. Altieri, M. Sanchez Portal, M. Kidger, and the Herschel Point Source Catalogue Working Group. The Herschel/PACS Point Source Catalogue Explanatory Supplement. *Herschel Highly Processed Data Products*, May 2017.

[44] J. S. Greaves, A. C. M. Whitelaw, and G. J. Bendo. The subsurface of Pluto from submillimetre observations. *MNRAS*, 449:L82–L85, April 2015.

[45] M. J. Griffin, A. Abergel, A. Abreu, P. A. R. Ade, P. André, J.-L. Augueres, T. Babbedge, Y. Bae, T. Baillie, J.-P. Baluteau, M. J. Barlow, G. Bendo, D. Benielli, J. J. Bock, P. Bonhomme, D. Brisbin, C. Brockley-Blatt, M. Caldwell, C. Cara, N. Castro-Rodriguez, R. Cerulli, P. Chanial, S. Chen, E. Clark, D. L. Clements, L. Clerc, J. Coker, D. Communal, L. Conversi, P. Cox, D. Crumb, C. Cunningham, F. Daly, G. R. Davis, P. de Antoni, J. Delderfield, N. Devin, A. di Giorgio, I. Didschuns, K. Dohlen, M. Donati, A. Dowell, C. D. Dowell, L. Duband, L. Dumaye, R. J. Emery, M. Ferlet, D. Ferrand, J. Fontignie, M. Fox, A. Franceschini, M. Frerking, T. Fulton, J. Garcia, R. Gastaud, W. K. Gear, J. Glenn, A. Goizel, D. K. Griffin, T. Grundy, S. Guest, L. Guillemet, P. C. Hargrave, M. Harwit, P. Hastings, E. Hatziminaoglou, M. Herman, B. Hinde, V. Hristov, M. Huang, P. Imhof, K. J. Isaak, U. Israelsson, R. J. Ivison, D. Jennings, B. Kiernan, K. J. King, A. E. Lange, W. Latter, G. Laurent, P. Laurent, S. J. Leeks, E. Lellouch, L. Levenson, B. Li, J. Li, J. Lilienthal, T. Lim, S. J. Liu, N. Lu, S. Madden, G. Mainetti, P. Marliani, D. McKay, K. Mercier, S. Molinari, H. Morris, H. Moseley, J. Mulder, M. Mur, D. A. Naylor, H. Nguyen, B. O'Halloran, S. Oliver, G. Olofsson, H.-G. Olofsson, R. Orfei, M. J. Page, I. Pain, P. Panuzzo, A. Papageorgiou, G. Parks, P. Parr-Burman, A. Pearce, C. Pearson, I. Pérez-Fournon, F. Pinsard, G. Pisano, J. Podosek, M. Pohlen, E. T. Polehampton, D. Pouliquen, D. Rigopoulou, D. Rizzo, I. G. Roseboom, H. Roussel, M. Rowan-Robinson, B. Rownd, P. Saraceno, M. Sauvage, R. Savage, G. Savini, E. Sawyer, C. Scharmberg, D. Schmitt, N. Schneider, B. Schulz, A. Schwartz, R. Shafer, D. L. Shupe, B. Sibthorpe, S. Sidher, A. Smith, A. J. Smith, D. Smith, L. Spencer, B. Stobie, R. Sudiwala, K. Sukhatme, C. Surace, J. A. Stevens, B. M. Swinyard, M. Trichas, T. Tourette, H. Triou, S. Tseng, C. Tucker, A. Turner, M. Vaccari, I. Valtchanov, L. Vigroux, E. Virique, G. Voellmer, H. Walker, R. Ward, T. Waskett, M. Weilert, R. Wesson, G. J. White, N. Whitehouse, C. D. Wilson, B. Winter, A. L. Woodcraft, G. S. Wright, C. K. Xu, A. Zavagno, M. Zemcov, L. Zhang, and E. Zonca. The Herschel-SPIRE instrument and its in-flight performance. *AAp*, 518:L3, July 2010.

[46] P. Hartogh, M. I. Błecka, C. Jarchow, H. Sagawa, E. Lellouch, M. de Val-Borro, M. Rengel, A. S. Medvedev, B. M. Swinyard, R. Moreno, T. Cavalié, D. C. Lis, M. Banaszkiewicz, D. Bockelée-Morvan, J. Crovisier, T. Encrenaz, M. Küppers, L.-M. Lara, S. Szutowicz, B. Vandenbussche, F. Bensch, E. A. Bergin, F. Billebaud, N. Biver, G. A. Blake, J. A. D. L. Blommaert, J. Cernicharo, L. Decin, P. Encrenaz, H. Feuchtgruber, T. Fulton, T. de Graauw, E. Jehin, M. Kidger, R. Lorente, D. A. Naylor, G. Portyankina, M. Sánchez-Portal, R. Schieder, S. Sidher, N. Thomas, E. Verdugo, C. Waelkens, A. Lorenzani, G. Tofani, E. Natale, J. Pearson, T. Klein, C. Leinz, R. Güsten, and C. Kramer. First results on Martian carbon monoxide from Herschel/HIFI observations. *AAp*, 521:L48, October 2010.

[47] P. Hartogh, C. Jarchow, E. Lellouch, M. de Val-Borro, M. Rengel, R. Moreno, A. S.

Medvedev, H. Sagawa, B. M. Swinyard, T. Cavalié, D. C. Lis, M. I. Błęcka, M. Banaszkiewicz, D. Bockelée-Morvan, J. Crovisier, T. Encrenaz, M. Küppers, L.-M. Lara, S. Szutowicz, B. Vandenbussche, F. Bensch, E. A. Bergin, F. Billebaud, N. Biver, G. A. Blake, J. A. D. L. Blommaert, J. Cernicharo, L. Decin, P. Encrenaz, H. Feuchtgruber, T. Fulton, T. de Graauw, E. Jehin, M. Kidger, R. Lorente, D. A. Naylor, G. Portyankina, M. Sánchez-Portal, R. Schieder, S. Sidher, N. Thomas, E. Verdugo, C. Waelkens, N. Whyborn, D. Teyssier, F. Helmich, P. Roelfsema, J. Stutzki, H. G. Leduc, and J. A. Stern. Herschel/HIFI observations of Mars: First detection of O_2 at submillimetre wavelengths and upper limits on HCl and H_2O_2. *AAp*, 521:L49, October 2010.

[48] P. Hartogh, E. Lellouch, R. Moreno, D. Bockelée-Morvan, N. Biver, T. Cassidy, M. Rengel, C. Jarchow, T. Cavalié, J. Crovisier, F. P. Helmich, and M. Kidger. Direct detection of the Enceladus water torus with Herschel. *AAp*, 532:L2, August 2011.

[49] P. Hartogh, D. C. Lis, D. Bockelée-Morvan, M. de Val-Borro, N. Biver, M. Küppers, M. Emprechtinger, E. A. Bergin, J. Crovisier, M. Rengel, R. Moreno, S. Szutowicz, and G. A. Blake. Ocean-like water in the Jupiter-family comet 103P/Hartley 2. *Nat*, 478:218–220, October 2011.

[50] R. Hopwood, E. T. Polehampton, I. Valtchanov, B. M. Swinyard, T. Fulton, N. Lu, N. Marchili, M. H. D. van der Wiel, D. Benielli, P. Imhof, J.-P. Baluteau, C. Pearson, D. L. Clements, M. J. Griffin, T. L. Lim, G. Makiwa, D. A. Naylor, G. Noble, E. Puga, and L. D. Spencer. Systematic characterization of the Herschel SPIRE Fourier Transform Spectrometer. *MNRAS*, 449:2274–2303, May 2015.

[51] Javier Gracía-Carpio, Michael Wetzstein, and Hélène Roussel. The JScanam Map-Maker Method Applied to Herschel/PACS Photometer Observations. *ASP Conf. Ser., Lorente, N. P. F. and Shortridge, K., Eds*, 2015.

[52] C. Kiss, T. G. Müller, M. Kidger, P. Mattisson, and G. Marton. Comet C/2013 A1 (Siding Spring) as seen with the Herschel Space Observatory. *AAp*, 574:L3, February 2015.

[53] C. Kiss, T. G. Müller, E. Vilenius, A. Pál, P. Santos-Sanz, E. Lellouch, G. Marton, E. Verebélyi, N. Szalai, P. Hartogh, J. Stansberry, F. Henry, and A. Delsanti. Optimized Herschel/PACS photometer observing and data reduction strategies for moving solar system targets. *Experimental Astronomy*, 37:161–174, July 2014.

[54] C. Kiss, A. Pál, A. I. Farkas-Takács, G. M. Szabó, R. Szabó, L. L. Kiss, L. Molnár, K. Sárneczky, T. G. Müller, M. Mommert, and J. Stansberry. Nereid from space: rotation, size and shape analysis from K2, Herschel and Spitzer observations. *MNRAS*, 457:2908–2917, April 2016.

[55] C. Kiss, G. Szabó, J. Horner, B. C. Conn, T. G. Müller, E. Vilenius, K. Sárneczky, L. L. Kiss, M. Bannister, D. Bayliss, A. Pál, S. Góbi, E. Verebélyi, E. Lellouch, P. Santos-Sanz, J. L. Ortiz, R. Duffard, and N. Morales. A portrait of the extreme solar system object 2012 DR_{30}. *AAp*, 555:A3, July 2013.

[56] M. Küppers, L. O'Rourke, D. Bockelée-Morvan, V. Zakharov, S. Lee, P. von Allmen, B. Carry, D. Teyssier, A. Marston, T. Müller, J. Crovisier, M. A. Barucci, and R. Moreno. Localized sources of water vapour on the dwarf planet (1) Ceres. *Nat*, 505:525–527, January 2014.

[57] P. Lacerda, S. Fornasier, E. Lellouch, C. Kiss, E. Vilenius, P. Santos-Sanz, M. Rengel, T. Müller, J. Stansberry, R. Duffard, A. Delsanti, and A. Guilbert-Lepoutre. The Albedo-Color Diversity of Transneptunian Objects. *ApJL*, 793:L2, September 2014.

[58] L. M. Lara, E. Lellouch, M. González, R. Moreno, and M. Rengel. A time-dependent photochemical model for Titan's atmosphere and the origin of H_2O. *AAp*, 566:A143, June 2014.

[59] E. Lellouch, P. Hartogh, H. Feuchtgruber, B. Vandenbussche, T. de Graauw, R. Moreno, C. Jarchow, T. Cavalié, G. Orton, M. Banaszkiewicz, M. I. Blecka, D. Bockelée-Morvan, J. Crovisier, T. Encrenaz, T. Fulton, M. Küppers, L. M. Lara, D. C. Lis, A. S. Medvedev, M. Rengel, H. Sagawa, B. Swinyard, S. Szutowicz, F. Bensch, E. Bergin, F. Billebaud, N. Biver, G. A. Blake, J. A. D. L. Blommaert, J. Cernicharo, R. Courtin, G. R. Davis, L. Decin, P. Encrenaz, A. Gonzalez, E. Jehin, M. Kidger, D. Naylor, G. Portyankina, R. Schieder, S. Sidher, N. Thomas, M. de Val-Borro, E. Verdugo, C. Waelkens, H. Walker, H. Aarts, C. Comito, J. H. Kawamura, A. Maestrini, T. Peacocke, R. Teipen, T. Tils, and K. Wildeman. First results of Herschel-PACS observations of Neptune. *AAp*, 518:L152, July 2010.

[60] E. Lellouch, C. Kiss, P. Santos-Sanz, T. G. Müller, S. Fornasier, O. Groussin, P. Lacerda, J. L. Ortiz, A. Thirouin, A. Delsanti, R. Duffard, A. W. Harris, F. Henry, T. Lim, R. Moreno, M. Mommert, M. Mueller, S. Protopapa, J. Stansberry, D. Trilling, E. Vilenius, A. Barucci, J. Crovisier, A. Doressoundiram, E. Dotto, P. J. Gutiérrez, O. Hainaut, P. Hartogh, D. Hestroffer, J. Horner, L. Jorda, M. Kidger, L. Lara, M. Rengel, B. Swinyard, and N. Thomas. "TNOs are cool": A survey of the trans-Neptunian region. II. The thermal lightcurve of (136108) Haumea. *AAp*, 518:L147, July 2010.

[61] E. Lellouch, R. Moreno, G. S. Orton, H. Feuchtgruber, T. Cavalié, J. I. Moses, P. Hartogh, C. Jarchow, and H. Sagawa. New constraints on the CH_4 vertical profile in Uranus and Neptune from Herschel observations. *AAp*, 579:A121, July 2015.

[62] E. Lellouch, P. Santos-Sanz, S. Fornasier, T. Lim, J. Stansberry, E. Vilenius, C. Kiss, T. Müller, G. Marton, S. Protopapa, P. Panuzzo, and R. Moreno. The long-wavelength thermal emission of the Pluto-Charon system from Herschel observations. Evidence for emissivity effects. *AAp*, 588:A2, April 2016.

[63] E. Lellouch, P. Santos-Sanz, P. Lacerda, M. Mommert, R. Duffard, J. L. Ortiz, T. G. Müller, S. Fornasier, J. Stansberry, C. Kiss, E. Vilenius, M. Mueller, N. Peixinho, R. Moreno, O. Groussin, A. Delsanti, and A. W. Harris. "TNOs are Cool": A survey of the trans-Neptunian region. IX. Thermal properties of Kuiper belt objects and Centaurs from combined Herschel and Spitzer observations. *AAp*, 557:A60, September 2013.

[64] J. Licandro, T. Müller, C. Alvarez, V. Alí-Lagoa, and M. Delbo. GTC/CanariCam observations of (99942) Apophis. *AAp*, 585:A10, January 2016.

[65] T. L. Lim, J. Stansberry, T. G. Müller, M. Mueller, E. Lellouch, C. Kiss, P. Santos-Sanz, E. Vilenius, S. Protopapa, R. Moreno, A. Delsanti, R. Duffard, S. Fornasier, O. Groussin, A. W. Harris, F. Henry, J. Horner, P. Lacerda, M. Mommert, J. L. Ortiz, M. Rengel, A. Thirouin, D. Trilling, A. Barucci, J. Crovisier, A. Doressoundiram, E. Dotto, P. J. Gutiérrez Buenestado, O. Hainaut, P. Hartogh, D. Hestroffer, M. Kidger, L. Lara, B. M. Swinyard, and N. Thomas. "TNOs are Cool": A survey

of the trans-Neptunian region . III. Thermophysical properties of 90482 Orcus and 136472 Makemake. *AAp*, 518:L148, July 2010.

[66] D. C. Lis, N. Biver, D. Bockelée-Morvan, P. Hartogh, E. A. Bergin, G. A. Blake, J. Crovisier, M. de Val-Borro, E. Jehin, M. Küppers, J. Manfroid, R. Moreno, M. Rengel, and S. Szutowicz. A Herschel Study of D/H in Water in the Jupiter-family Comet 45P/Honda-Mrkos-Pajdušáková and Prospects for D/H Measurements with CCAT. *ApJL*, 774:L3, September 2013.

[67] G. Marton, C. Kiss, Z. Balog, E. Lellouch, E. Verebélyi, and U. Klaas. Search for signatures of dust in the Pluto-Charon system using Herschel/PACS observations. *AAp*, 579:L9, July 2015.

[68] K. J. Meech, M. F. A'Hearn, J. A. Adams, P. Bacci, J. Bai, L. Barrera, M. Battelino, J. M. Bauer, E. Becklin, B. Bhatt, N. Biver, D. Bockelée-Morvan, D. Bodewits, H. Böhnhardt, J. Boissier, B. P. Bonev, W. Borghini, J. R. Brucato, E. Bryssinck, M. W. Buie, H. Canovas, D. Castellano, S. B. Charnley, W. P. Chen, P. Chiang, Y.-J. Choi, D. J. Christian, Y.-L. Chuang, A. L. Cochran, P. Colom, M. R. Combi, I. M. Coulson, J. Crovisier, N. Dello Russo, K. Dennerl, K. DeWahl, M. A. DiSanti, M. Facchini, T. L. Farnham, Y. Fernández, H. G. Florén, U. Frisk, T. Fujiyoshi, R. Furusho, T. Fuse, G. Galli, D. A. García-Hernández, A. Gersch, Z. Getu, E. L. Gibb, M. Gillon, E. Guido, R. A. Guillermo, E. Hadamcik, O. Hainaut, H. B. Hammel, D. E. Harker, J. K. Harmon, W. M. Harris, P. Hartogh, M. Hashimoto, B. Häusler, T. Herter, A. Hjalmarson, S. T. Holland, M. Honda, S. Hosseini, E. S. Howell, N. Howes, H. H. Hsieh, H.-Y. Hsiao, D. Hutsemékers, S. M. Immler, W. M. Jackson, S. V. Jeffers, E. Jehin, T. J. Jones, M. de Juan Ovelar, H. M. Kaluna, T. Karlsson, H. Kawakita, J. V. Keane, L. D. Keller, M. S. Kelley, D. Kinoshita, N. N. Kiselev, J. Kleyna, M. M. Knight, H. Kobayashi, H. A. Kobulnicky, L. Kolokolova, M. Kreiny, Y.-J. Kuan, M. Küppers, J. M. Lacruz, W. B. Landsman, L. M. Lara, A. Lecacheux, A. C. Levasseur-Regourd, B. Li, J. Licandro, R. Ligustri, Z.-Y. Lin, M. Lippi, D. C. Lis, C. M. Lisse, A. J. Lovell, S. C. Lowry, H. Lu, S. Lundin, K. Magee-Sauer, P. Magain, J. Manfroid, E. Mazzotta Epifani, A. McKay, M. D. Melita, H. Mikuz, S. N. Milam, G. Milani, M. Min, R. Moreno, B. E. A. Mueller, M. J. Mumma, M. Nicolini, M. C. Nolan, H. L. Nordh, P. B. Nowajewski, Odin Team, T. Ootsubo, L. Paganini, C. Perrella, J. Pittichová, E. Prosperi, Y. L. Radeva, W. T. Reach, A. J. Remijan, M. Rengel, T. E. Riesen, M. Rodenhuis, D. P. Rodríguez, R. W. Russell, D. K. Sahu, N. H. Samarasinha, A. Sánchez Caso, A. Sandqvist, G. Sarid, M. Sato, D. G. Schleicher, E. W. Schwieterman, A. K. Sen, D. Shenoy, J.-C. Shi, Y. Shinnaka, J. Skvarc, C. Snodgrass, M. L. Sitko, S. Sonnett, S. Sosseini, G. Sostero, S. Sugita, B. M. Swinyard, S. Szutowicz, N. Takato, P. Tanga, P. A. Taylor, G.-P. Tozzi, R. Trabatti, J. M. Trigo-Rodríguez, C. Tubiana, M. de Val-Borro, W. Vacca, B. Vandenbussche, J. Vaubaillion, F. P. Velichko, S. F. Velichko, R. J. Vervack, Jr., M. J. Vidal-Nunez, G. L. Villanueva, C. Vinante, J.-B. Vincent, M. Wang, L. H. Wasserman, J. Watanabe, H. A. Weaver, P. R. Weissman, S. Wolk, D. H. Wooden, C. E. Woodward, M. Yamaguchi, T. Yamashita, P. A. Yanamandra-Fischer, B. Yang, J.-S. Yao, D. K. Yeomans, T. Zenn, H. Zhao, and J. E. Ziffer. EPOXI: Comet 103P/Hartley 2 Observations from a Worldwide Campaign. *ApJL*, 734:L1, June 2011.

[69] M. Mommert, A. W. Harris, C. Kiss, A. Pál, P. Santos-Sanz, J. Stansberry, A. Delsanti, E. Vilenius, T. G. Müller, N. Peixinho, E. Lellouch, N. Szalai, F. Henry, R. Duffard, S. Fornasier, P. Hartogh, M. Mueller, J. L. Ortiz, S. Protopapa, M. Rengel, and

A. Thirouin. TNOs are cool: A survey of the trans-Neptunian region. V. Physical characterization of 18 Plutinos using Herschel-PACS observations. *AAp*, 541:A93, May 2012.

[70] R. Moreno, E. Lellouch, L. M. Lara, R. Courtin, D. Bockelée-Morvan, P. Hartogh, M. Rengel, N. Biver, M. Banaszkiewicz, and A. González. First detection of hydrogen isocyanide (HNC) in Titan's atmosphere. *AAp*, 536:L12, December 2011.

[71] R. Moreno, E. Lellouch, L. M. Lara, H. Feuchtgruber, M. Rengel, P. Hartogh, and R. Courtin. The abundance, vertical distribution and origin of H_2O in Titan's atmosphere: Herschel observations and photochemical modelling. *icarus*, 221:753–767, November 2012.

[72] T. Müller, Z. Balog, M. Nielbock, T. Lim, D. Teyssier, M. Olberg, U. Klaas, H. Linz, B. Altieri, C. Pearson, G. Bendo, and E. Vilenius. Herschel celestial calibration sources. Four large main-belt asteroids as prime flux calibrators for the far-IR/submm range. *Experimental Astronomy*, 37:253–330, July 2014.

[73] T. G. Müller, Z. Balog, M. Nielbock, R. Moreno, U. Klaas, A. Moór, H. Linz, and H. Feuchtgruber. Far-infrared photometric observations of the outer planets and satellites with Herschel-PACS. *AAp*, 588:A109, April 2016.

[74] T. G. Müller, C. Kiss, P. Scheirich, P. Pravec, L. O'Rourke, E. Vilenius, and B. Altieri. Thermal infrared observations of asteroid (99942) Apophis with Herschel. *AAp*, 566:A22, June 2014.

[75] T. G. Müller, E. Lellouch, J. Stansberry, C. Kiss, P. Santos-Sanz, E. Vilenius, S. Protopapa, R. Moreno, M. Mueller, A. Delsanti, R. Duffard, S. Fornasier, O. Groussin, A. W. Harris, F. Henry, J. Horner, P. Lacerda, T. Lim, M. Mommert, J. L. Ortiz, M. Rengel, A. Thirouin, D. Trilling, A. Barucci, J. Crovisier, A. Doressoundiram, E. Dotto, P. J. Gutiérrez, O. R. Hainaut, P. Hartogh, D. Hestroffer, M. Kidger, L. Lara, B. Swinyard, and N. Thomas. "TNOs are Cool": A survey of the trans-Neptunian region. I. Results from the Herschel science demonstration phase (SDP). *AAp*, 518:L146, July 2010.

[76] T. G. Müller, T. Miyata, C. Kiss, M. A. Gurwell, S. Hasegawa, E. Vilenius, S. Sako, T. Kamizuka, T. Nakamura, K. Asano, M. Uchiyama, M. Konishi, M. Yoneda, T. Ootsubo, F. Usui, Y. Yoshii, M. Kidger, B. Altieri, R. Lorente, A. Pál, L. O'Rourke, and L. Metcalfe. Physical properties of asteroid 308635 (2005 YU_{55}) derived from multi-instrument infrared observations during a very close Earth approach. *AAp*, 558:A97, October 2013.

[77] T. G. Müller, L. O'Rourke, A. M. Barucci, A. Pál, C. Kiss, P. Zeidler, B. Altieri, B. M. González-García, and M. Küppers. Physical properties of OSIRIS-REx target asteroid (101955) 1999 RQ_{36}. Derived from Herschel, VLT/ VISIR, and Spitzer observations. *AAp*, 548:A36, December 2012.

[78] Babar Ali; Bruno Altieri; Zoltan Balog; Alexandre Beelen; Stefano Berta; Pierre Chanial; Javier Gracia-Carpio; Vera Knyves; Gabor Marton; Roberta Paladini; Pasquale Panuzzo; Lorenzo Piazzo; Helene Roussel; Roland Vavrek; Michael WetzsteinKatrina Exter (Alphabetical order. PACS Map-making Tools: Analysis and Benchmarking. *Herschel Space Observatory - PACS Herschel*, 2013.

[79] L. O'Rourke, D. Bockelée-Morvan, N. Biver, B. Altieri, D. Teyssier, L. Jorda, V. De-

bout, C. Snodgrass, M. Küppers, M. A'Hearn, T. G. Müller, and T. Farnham. Herschel and IRAM-30 m observations of comet C/2012 S1 (ISON) at 4.5 AU from the Sun. *AAp*, 560:A101, December 2013.

[80] L. O'Rourke, T. Müller, I. Valtchanov, B. Altieri, B. M. González-Garcia, B. Bhattacharya, L. Jorda, B. Carry, M. Küppers, O. Groussin, K. Altwegg, M. A. Barucci, D. Bockelee-Morvan, J. Crovisier, E. Dotto, P. Garcia-Lario, M. Kidger, A. Llorente, R. Lorente, A. P. Marston, M. Sanchez Portal, R. Schulz, M. Sierra, D. Teyssier, and R. Vavrek. Thermal and shape properties of asteroid (21) Lutetia from Herschel observations around the Rosetta flyby. *PlanSS*, 66:192–199, June 2012.

[81] L. O'Rourke, C. Snodgrass, M. de Val-Borro, N. Biver, D. Bockelée-Morvan, H. Hsieh, D. Teyssier, Y. Fernandez, M. Kueppers, M. Micheli, and P. Hartogh. Determination of an Upper Limit for the Water Outgassing Rate of Main-belt Comet P/2012 T1 (PANSTARRS). *ApJL*, 774:L13, September 2013.

[82] P. Popesso, B. Magnelli, S. Buttiglione, D. Lutz, R. Nordon A. Poglitsch, B. Altieri, H. Aussel, N. Billot, R. Gastaud, B. Ali, Z. Balog, A. Cava, H. Feuchtgruber, B. Gonzalez Garcia, N. Geis, C. Kiss, U. Klaas, H. Linz, X. C. Liu, A. Moor, B. Morin, T. Müller, M. Nielbock, K. Okumura, S. Osterhage, R. Ottensamer, R. Paladini, S. Pezzuto, V. Dublier Pritchard, S. Regibo, G. Rodighiero, P. Royer, M. Sauvage, E. Sturm, M. Wetzstein, E. Wieprecht, and E.Wiezorrek. The effect of the high-pass filter data reduction technique on the Herschel PACS Photometer PSF and noise. *A&A*, page A32, November 2012.

[83] A. Pál, C. Kiss, J. Horner, R. Szakáts, E. Vilenius, T. G. Müller, J. Acosta-Pulido, J. Licandro, A. Cabrera-Lavers, K. Sárneczky, G. M. Szabó, A. Thirouin, B. Sipőcz, Á. Dózsa, and R. Duffard. Physical properties of the extreme Centaur and supercomet candidate 2013 AZ_{60}. *AAp*, 583:A93, November 2015.

[84] A. Pál, C. Kiss, T. G. Müller, P. Santos-Sanz, E. Vilenius, N. Szalai, M. Mommert, E. Lellouch, M. Rengel, P. Hartogh, S. Protopapa, J. Stansberry, J.-L. Ortiz, R. Duffard, A. Thirouin, F. Henry, and A. Delsanti. "TNOs are Cool": A survey of the trans-Neptunian region. VII. Size and surface characteristics of (90377) Sedna and 2010 EK_{139}. *AAp*, 541:L6, May 2012.

[85] L. Piazzo, L. Calzoletti, F. Faustini, M. Pestalozzi, S. Pezzuto, D. Elia, A. di Giorgio, and S. Molinari. UNIMAP: a generalized least-squares map maker for Herschel data. *MNRAS*, 447:1471–1483, February 2015.

[86] G. L. Pilbratt et al. Herschel Space Observatory - An ESA facility for far-infrared and submillimetre astronomy. *AAp*, 518:L1, 2010.

[87] Pilbratt, G. L., Riedinger, J. R., Passvogel, T., Crone, G., Doyle, D., Gageur, U., Heras, A. M., Jewell, C., Metcalfe, L., Ott, S., and Schmidt, M. Herschel Space Observatory* - An ESA facility for far-infrared and submillimetre astronomy. *A& A*, 518:L1, 2010.

[88] M. Rengel, H. Sagawa, P. Hartogh, E. Lellouch, H. Feuchtgruber, R. Moreno, C. Jarchow, R. Courtin, J. Cernicharo, and L. M. Lara. Herschel/PACS spectroscopy of trace gases of the stratosphere of Titan. *AAp*, 561:A4, January 2014.

[89] W Romanishin. An Introduction to Astronomical Photometry Using CCDs. 04 2018.

[90] H. Roussel. Scanamorphos: A Map-making Software for Herschel and Similar Scanning Bolometer Arrays. *PASP*, 125:1126, September 2013.

[91] Katrina Exter; Zoltan Balog; Luca Calzoletti; Ulrich Klaas; Dieter Lutz; Roberta Paladini; Elena Puga; Pierre Royer. The Photodetector Array Camara and Spectrometer (PACS) Handbook. *Herschel Explanatory Supplement*, III, 2017.

[92] Miguel Sanchez-Portal, A Marston, Bruno Altieri, Herve Aussel, Helmut Feuchtgruber, Ulrich Klaas, Hendrik Linz, Dieter Lutz, Bruno Mern, T Mueller, Markus Nielbock, Marc Oort, Gran Pilbratt, Micha Schmidt, Craig Stephenson, and Mark Tuttlebee. The pointing system of the herschel space observatory. *Experimental Astronomy*, 37:453–479, 07 2014.

[93] P. Santos-Sanz, E. Lellouch, S. Fornasier, C. Kiss, A. Pal, T. G. Müller, E. Vilenius, J. Stansberry, M. Mommert, A. Delsanti, M. Mueller, N. Peixinho, F. Henry, J. L. Ortiz, A. Thirouin, S. Protopapa, R. Duffard, N. Szalai, T. Lim, C. Ejeta, P. Hartogh, A. W. Harris, and M. Rengel. "TNOs are Cool": A survey of the trans-Neptunian region. IV. Size/albedo characterization of 15 scattered disk and detached objects observed with Herschel-PACS. *AAp*, 541:A92, May 2012.

[94] James H. Shirley. *Solar Constant*, pages 666–667. Springer Netherlands, Dordrecht, 2005.

[95] B. M. Swinyard, E. T. Polehampton, R. Hopwood, I. Valtchanov, N. Lu, T. Fulton, D. Benielli, P. Imhof, N. Marchili, J.-P. Baluteau, G. J. Bendo, M. Ferlet, M. J. Griffin, T. L. Lim, G. Makiwa, D. A. Naylor, G. S. Orton, A. Papageorgiou, C. P. Pearson, B. Schulz, S. D. Sidher, L. D. Spencer, M. H. D. van der Wiel, and R. Wu. Calibration of the Herschel SPIRE Fourier Transform Spectrometer. *MNRAS*, 440:3658–3674, June 2014.

[96] G. M. Szabó, L. L. Kiss, A. Pál, C. Kiss, K. Sárneczky, A. Juhász, and M. R. Hogerheijde. Evidence for Fresh Frost Layer on the Bare Nucleus of Comet Hale-Bopp at 32 AU Distance. *ApJ*, 761:8, December 2012.

[97] U. Klaas T. Muller, K. Okumura. PACS Photometer Passbands and Colour Correction Factors for Various Source SEDs. *PACS Herschel - PACS Photometer - Colour Corrections*, 2011.

[98] N. A. Teanby, P. G. J. Irwin, C. A. Nixon, R. Courtin, B. M. Swinyard, R. Moreno, E. Lellouch, M. Rengel, and P. Hartogh. Constraints on Titan's middle atmosphere ammonia abundance from Herschel/SPIRE sub-millimetre spectra. *PlanSS*, 75:136–147, January 2013.

[99] N. A. Teanby, A. P. Showman, L. N. Fletcher, and P. G. J. Irwin. Constraints on Jupiter's stratospheric HCl abundance and chlorine cycle from Herschel/HIFI. *PlanSS*, 103:250–261, November 2014.

[100] David Teyssier. Quick-Start Guide To Herschel-HIFI. *Herschel Space Observatory*, 2018.

[101] I. Valtchanov, R. Hopwood, E. Polehampton, D. Benielli, T. Fulton, P. Imhof, T. Konopczyński, T. Lim, N. Lu, N. Marchili, D. Naylor, and B. Swinyard. Relative pointing offset analysis of calibration targets with repeated observations with Herschel-SPIRE Fourier-transform spectrometer. *Experimental Astronomy*, 37:207–223, July 2014.

[102] Ivan Valtchanov. Quick-Start Guide To Herschel-SPIRE. *Herschel Space Observatory*, 2017.

[103] E. Vilenius, C. Kiss, M. Mommert, T. Müller, P. Santos-Sanz, A. Pal, J. Stansberry, M. Mueller, N. Peixinho, S. Fornasier, E. Lellouch, A. Delsanti, A. Thirouin, J. L. Ortiz, R. Duffard, D. Perna, N. Szalai, S. Protopapa, F. Henry, D. Hestroffer, M. Rengel, E. Dotto, and P. Hartogh. "TNOs are Cool": A survey of the trans-Neptunian region. VI. Herschel/PACS observations and thermal modelling of 19 classical Kuiper belt objects. *AAp*, 541:A94, May 2012.

[104] E. Vilenius, C. Kiss, T. Müller, M. Mommert, P. Santos-Sanz, A. Pál, J. Stansberry, M. Mueller, N. Peixinho, E. Lellouch, S. Fornasier, A. Delsanti, A. Thirouin, J. L. Ortiz, R. Duffard, D. Perna, and F. Henry. "TNOs are Cool": A survey of the trans-Neptunian region. X. Analysis of classical Kuiper belt objects from Herschel and Spitzer observations. *AAp*, 564:A35, April 2014.

[105] R. Wu, E. T. Polehampton, M. Etxaluze, G. Makiwa, D. A. Naylor, C. Salji, B. M. Swinyard, M. Ferlet, M. H. D. van der Wiel, A. J. Smith, T. Fulton, M. J. Griffin, J.-P. Baluteau, D. Benielli, J. Glenn, R. Hopwood, P. Imhof, T. Lim, N. Lu, P. Panuzzo, C. Pearson, S. Sidher, and I. Valtchanov. Observing extended sources with the Herschel SPIRE Fourier Transform Spectrometer. *AAp*, 556:A116, August 2013.

[106] L. Yu and J. Ji. Surface thermophysical properties determination of OSIRIS-REx target asteroid (101955) Bennu. *MNRAS*, 452:368–375, September 2015.

Appendix

A List of Acronyms

ADP	Ancillary Data Products
AOR	Astronomical Observation Request
AOT	Astronomical Observation Template
AU	Astronomical Unit
CC	Colour Corrected
CCD	Charged-Coupled Device
DDT	Director's Discretionary Time
DO	Detached Objects
EMR	Electromagnetic Radiation
ESA	European Space Agency
FIR	Far-Infrared Radiation
FITS	Flexible Image Transport System
FoV	Field of View
FWHM	Full Width at Half Maximum
GT	Guaranteed Time
GUI	Graphical User Interface
HCSSOO	Herschel Catalogue of Solar System Object Observations
HEB	Hot Electron Bolometer
HIFI	Heterodyne Instrument for the Far Infrared
HIPE	Herschel Interactive Processing Environment
HPDP	Highly Processed Data Products
HPF	High-Pass Filtering
HPPPMB	Herschel PACS Photometer PhotProject MAP Blue
HPPPMR	Herschel PACS Photometer PhotProject MAP Red
HPPSC	Herschel/PACS Point Source Catalogue
HSA	Herschel Science Archive
HSC	Herschel Science Centre
HSPSC	Herschel/SPIRE Point Source Catalogue
IAU	International Astronomical Union
IR	Infrared Radiation
JAXA	Japan Aerospace Exploration Agency
JPL	Jet Propulsion Laboratory
MBA	Main Belt Asteroid
MBC	Main Belt Comet
mJy	milliJansky
MOID	Minimum Orbit Intersection Distance
NA	Not Available
NASA	National Aeronautics and Space Administration
NEA	Near-Earth Asteroid
NEO	Near-Earth Object
OT	Open Time
PACS	Photoconductor Array Camera and Spectrometer
PHO	Potentially Hazardous Object
PSF	Point Spread Function

PV	Performance Verification
RMS	Root Mean Square
SDO	Scattered Disk Object
SED	Spectral Energy Distribution
SIS	Superconductors-Insulator-Superconductor
SPG	Standard Product Generation
SPIRE	Spectral and Photometric Imaging Receiver
SS	Solar System
SSO	Solar System Object
SSOO	Solar System Object Observations
sub-mm	submillimetre
TNO	Trans-Neptunian Object
UPDP	User Provided Data Products

B Index Publications of Herschel Observations

1. [56]
2. [72]
3. [77]
4. [106]
5. [41]
6. [57]
7. [40]
8. [53]
9. [37]
10. [36]
11. [103]
12. [63]
13. [93]
14. [69]
15. [75]
16. [104]
17. [60]
18. [65]
19. [84]
20. [55]
21. [83]
22. [80]
23. [26]
24. [74]
25. [64]
26. [35]
27. [31]
28. [76]
29. [30]
30. [28]
31. [96]
32. [68]
33. [29]
34. [49]
35. [66]
36. [79]
37. [32]
38. [99]
39. [46]
40. [47]
41. [59]
42. [61]
43. [39]
44. [95]
45. [101]
46. [50]
47. [54]
48. [73]
49. [81]
50. [44]
51. [62]
52. [67]
53. [48]
54. [105]
55. [52]
56. [27]
57. [71]
58. [70]
59. [58]
60. [98]
61. [34]
62. [88]
63. [33]